

INTERFACE ORIENTATION DEPENDENT FIELD EVAPORATION
BEHAVIOR IN MULTILAYER
THIN FILMS

by

JUSTIN GLEN BRONS

A THESIS

Submitted in partial fulfillment of the requirements for the degree
of Master of Science in the Department of
Metallurgical and Materials Engineering
in the Graduate School of
The University of Alabama

TUSCALOOSA, ALABAMA

2011

Copyright Justin Glen Brons 2011
ALL RIGHTS RESERVED

ABSTRACT

In general, atom probe reconstruction algorithms assume a constant evaporation field across the surface of the specimen. In reality, chemical inhomogeneity modulates the evaporation field at the specimen surface, which introduces reconstruction artifacts and degrades the spatial resolution of the atom probe tomography (APT) technique. Multilayer thin films provide ideal specimen geometries to measure and quantify these artifacts. Thin films can be deposited with near atomic layer precision and can exhibit large planar surfaces with degrees of intermixing across the interfaces. Quantifying and rectifying interfacial compositional differences in atom probe data sets is critical, as such information can be used to understand the growth and intermixing of species in nanolaminate devices, such as giant magneto-resistance multilayers.

A series of Fe/Ni and Ti/Nb multilayers featuring a bilayer repeat unit of equal thickness and repeat distance of approximately 4 nm have been sputter-deposited onto n-doped Si [001] substrates. The multilayers were focus ion beam (FIB) milled with an annular milling geometry into the required needle-shaped geometry for the APT analysis. Specimens were prepared with the film interfaces oriented with the chemical modulations for a given bilayer spacing parallel and perpendicular to the specimen apex to compare field evaporation behavior at these limiting geometries.

For the Fe/Ni multilayers, the 4 nm bilayer films exhibited Fe intermixing within the Ni layers. The Electron Energy Loss Spectroscopy (EELS) based compositional profiles were used

in order to cross-correlate across the two techniques using a chemical comparison. These profiles were acquired using aberration-corrected scanning transmission electron microscopy (STEM) with an approximate 100 pm electron probe. The slope of the compositional gradients between the layered interfaces showed very little differences between the EELS and atom probe data sets for Fe/Ni. In addition, little difference was observed between the parallel and perpendicular field evaporation limiting geometries. This has been contributed to Fe and Ni having a similar elemental evaporation field strength of 33 and 35 V/nm.

The Fe/Ni results were compared to data obtained from a Ti/Nb multilayered thin film with a bilayer spacing of approximately 4 nm, prepared in similar parallel and perpendicular evaporation orientations as those discussed above. Compositional EELS profiles were collected using an aberration-corrected scanning transmission electron microscopy (STEM) with an approximate 100 pm electron probe. The slope of the compositional gradients between the layered interfaces showed very little differences between the EELS and atom probe data sets for Ti/Nb. In the perpendicular evaporation orientation, it was found that the layer thicknesses for both the Ti and Nb elemental layers were measured at values closer to the actual specimen, while the perpendicular orientation contained reconstruction artifacts that compressed the layer thicknesses.

The EELS based compositional profiles were used in order to cross correlate across the two techniques using a chemical comparison. The compositional gradient across the interfaces was also closer to the true value in the parallel orientation, while the perpendicular orientation contained artifacts that altered the composition across the compressed interfaces. This study

showed in the atom probe data there was upwards of 20 atomic % Nb was intermixed in the Ti layers. This finding was verified by the EELS compositional profiles.

DEDICATION

This thesis is for my friends at home for always being there for me and encouraging me to follow my dreams. It is for my fraternity at Virginia Tech and all of my brothers for instilling me with the drive and motivation to help me do my work, fulfill my obligations, and bring about that happy life wherein I may more truly love my fellow man. It is also for my family and my support system at home, for always having my back and being there for me when times were the hardest. This thesis would not have been possible without all of you, and my love goes out to all of you because of that.

LIST OF ABBREVIATIONS AND SYMBOLS

APT	Atom probe tomography
EELS	Electron energy loss spectroscopy
TEM	Transmission electron microscope
Co	Cobalt
Cr	Chromium
Tb	Terbium
Fe	Iron
Sm	Samarium
Al	Aluminum
Si	Silicon
Ge	Germanium
nm	Nanometer
FIM	Field ion microscope
Pa	Pascals
APFIM	Atom probe field ion microscope
mm	Millimeter
LEAP	Local electrode atom probe
kHz	Kilohertz
η	Magnification

ξ	Image compression factor
r	Radius of curvature
F	Evaporation field at the specimen apex
K	Geometrical Factor
V	Applied voltage
eV	Electron volt
v	Ion velocity
t	Time-of-flight
α	Pulse amplitude coupling factor
amu	Atomic mass units
%	Percent
EDS	Energy dispersive spectroscopy
WDS	Wavelength dispersive spectroscopy
STEM	Scanning transmission electron microscopy
E_0	Energy of electrons with no energy loss
Δ	Change in
>	Greater than
<	Less than
Ni	Nickel
Ti	Titanium
Nb	Niobium

cm	Centimeter
~	Approximately
XRR	X-ray reflectivity
XRD	X-ray diffraction
FIB	Focused ion beam
FIB-SEM	Focused ion beam scanning electron microscope
LMIS	Liquid metal ion source
°	Degree
GIS	Gas injection system
Pt	Platinum
Ar	Argon
PIPS	Precision ion polishing system
d	Lattice spacing
R	Measured radial projection
λ	Electron wavelength
L	Camera length
NIST	National Institute of Standards and Technology
HAADF	High angle annular dark field
N	Newtons
m	Meter
μm	Micrometers

K	Degrees Kelvin
Cu	Copper
SRIM	Stopping and range of ions in matter
TOF	Time-of-flight

ACKNOWLEDGMENTS

I am pleased to have this opportunity to thank the many colleagues, friends, and faculty members who have helped me with this research project. I am most indebted to Professor Gregory Thompson, the chairman of this thesis, for sharing his research expertise and wisdom regarding motivational theory. I would also like to thank all of my committee members, Professors Gary Mankey and Nitin Chopra as well as Professor Viola Acoff, the department head for the Metallurgical Engineering Department for their invaluable input, inspiring questions, and support of both the dissertation and my academic progress.

I would like to recognize the National Science Foundation for their financial support for my research through grant numbers EPS08-14103 and DMR-0529369. I appreciate the use of the general user facilities within the Central Analytical Facility (CAF) and the facilities of the Center for Materials for Information Technology (MINT). I would like to thank my collaborators at the National Institute for Standards and Technology (NIST): Dr. Ian Anderson and Dr. Andrew Herzing.

I would like to thank my fellow colleagues: Dr. Karen Henry, Mr. Bianzhu Fu, and Mr. Chad Hornbuckle for helpful discussions on atom probe reconstructions and in-situ tip shape formation, Dr. Robert Morris and Mr. Nicholas De Leon for discussions relating to TEM micrograph interpretation, the graduate students in Thompson's Research Group, and a special thanks to the Department of Metallurgical Engineering and CAF Staff for all the background work that kept my research productive.

CONTENTS

ABSTRACT	ii
DEDICATION	v
LIST OF ABBREVIATIONS AND SYMBOLS	vi
ACKNOWLEDGMENTS	x
LIST OF TABLES	xiv
LIST OF FIGURES	xv
1. INTRODUCTION	1
1.1 Atom Probe Tomography	1
1.2 Multilayered Thin Films	5
1.3 Application of APT in Thin Films	5
1.4 Development of APT	7
1.5 Atom Probe Reconstruction	13
1.6 Electron Energy Loss Spectroscopy	15
1.7 Electron Energy Loss Spectrum.....	18
2. EXPERIMENTAL.....	21
2.1 Sputter Deposition	21
2.2 Analytical Instruments	24
2.2.1 FIB Overview—TEM Foil Preparation	24

2.2.2 TEM Phase Identification	28
2.2.3 STEM-EELS Analysis	28
2.2.4 APT Sample Preparation.....	32
2.2.4.1 Perpendicular APT Sample Preparation	32
2.2.4.2 Parallel APT Sample Preparation	36
2.2.5 Atom Probe Tomography	38
2.3 TEM Correlation of APT Evaporation	38
2.4 Experimental Evaporation Simulations	39
2.4.1 TipSim	39
2.4.2 SRIM.....	41
3. RESULTS	43
3.1 TEM Phase Identification	43
3.2 Electron Energy Loss Spectroscopy	45
3.3 APT in the Perpendicular Orientation.....	50
3.4 APT in the Parallel Orientation.....	57
4. DISCUSSION	65
4.1 Phase Change as a Function of Multilayering	65
4.2 Cross-Correlation Comparisons Between EELS and APT	66
4.2.1 Correlation Between Perpendicular APT and EELS	66
4.2.2 Correlation Between Parallel APT and EELS	70
4.2.3 Correlation Between Perpendicular and Parallel APT.....	73

4.3 Reconstruction Artifacts Explained by Tip Shape Evolution	75
4.4 TipSim Evaporation Simulations	76
4.5 Orientation Dependent Intermixing	82
5. CONCLUSION AND FUTURE WORK	92
6. REFERENCES	96

LIST OF TABLES

3.1 Measured Elemental Layer Thicknesses from Different Techniques..47

4.1 Correlation of Compositional Gradients Across Techniques69

LIST OF FIGURES

1.1 Preferential Evaporation due to Different Evaporation Fields	3
1.2 Atom Probe Tomography Limiting Geometries	3
1.3 Local Electrode Atom Probe Schematic	10
1.4 Electron Energy Loss Spectroscopy Schematic.....	17
1.5 Typical EELS Energy Loss Spectrum	19
2.1 AJA ATC-1500 Stainless Steel Magnetron Sputtering Chamber.....	22
2.2 LABVIEW® User System Interface	23
2.3 Schematic of FEI Quanta 3D Dual Beam FIB.....	25
2.4 Schematic of TEM Foil Lift-Out Procedure	27
2.5 EELS Spectrum for the Fe/Ni ~4 nm Bilayer Film	30
2.6 Cameca® LEAP 3000XSi	33
2.7 APT In-Situ Tip Preparation, Perpendicular Orientation	34
2.8 APT In-Situ Tip Preparation, Parallel Orientation	37
2.9 APT Tip Extraction for TEM Analysis.....	40
3.1 Multi-Crystalline TEM Selected Area Diffraction Patterns	44
3.2 HAADF-STEM Images of the Fe/Ni and Ti/Nb Films	44
3.3 Fe/Ni EELS Compositional Profile	46
3.4 Ti/Nb EELS Areal Density Core-Loss Profile.....	49
3.5 APT Voltage History from the Perpendicular Orientations.....	51

3.6 APT Corrected TOF Spectrums of Perpendicular Orientations	52
3.7 APT Mass Spectrums of Perpendicular Orientations	53
3.8 APT Atom Maps from the Perpendicular Orientations	54
3.9 Fe/Ni Perpendicular APT Proximity Histogram.....	55
3.10 Ti/Nb Perpendicular APT Proximity Histogram	56
3.11 APT Voltage History from the Parallel Orientations.....	58
3.12 APT Corrected TOF Spectrums from the Parallel Orientations	59
3.13 APT Mass Spectrums from the Parallel Orientations	60
3.14 APT Atom Maps from the Parallel Orientations	61
3.15 Fe/Ni Parallel APT Proximity Histogram.....	62
3.16 Ti/Nb Parallel APT Proximity Histogram	64
4.1 APT Tip Shape Evolutions	68
4.2 TipSim Fe/Ni Reconstruction in the Perpendicular Orientation.....	78
4.3 TipSim Fe/Ni Reconstruction in the Parallel Orientation.....	79
4.4 TipSim Ti/Nb Reconstruction in the Perpendicular Orientation	80
4.5 TipSim Ti/Nb Reconstruction in the Parallel Orientation	81
4.6 Orientation Dependent Ga Ion Beam Damage	83
4.7 APT Reconstructed Atom Maps with Gallium Damage.....	85
4.8 SRIM Simulations (Fe/Ni vs Ti/Nb) Ion Trajectories	86
4.9 SRIM Simulations (Fe/Ni vs Ti/Nb) Collision Events	88
4.10 SRIM Simulations of Ion Trajectories with Pt Cap.....	89

4.11 SRIM Simulations of Collision Events with Pt Cap.....	90
--	----

CHAPTER 1

INTRODUCTION

1.1 Atom Probe Tomography

One way that scientists are able to visualize and quantify the positions of atoms within a material is by the use of atom probe tomography. Atom probe tomography (APT) uses field evaporation from both voltage and laser energy pulses in conjunction with a time-of-flight position-sensitive detector in order to identify the element and the position of the evaporated ion [1]. Many software programs have been written and are being sold commercially in order to reconstruct all of this data into a digital recreation of the specimen, atom-by-atom. These reconstruction software programs use a reconstruction algorithm that assumes a constant evaporation field across the surface of the specimen. In reality, because of layer interfaces, precipitate particles, grain boundaries, and surfaces, this assumption does not hold true for all points within a specimen.

Research has been performed by Vurpillot, Marquis, Larson, and others in order to alter the way data is reconstructed to perfect the placement of the atoms within the digital atom map [2-4]. To date, there is no one program or algorithm in place that can allow for this digital reconstruction of the specimen to be perfect. When the reconstruction deviates from the actual atomic spatial position within the specimen, this is known as an artifact within the reconstruction. Most artifacts found in reconstructions are generated as a result of experimental constraints within the experiment, such as the physics behind field strength for evaporation

between the two different atoms. Two of these issues observed most commonly are known as local magnification and preferential evaporation [4]. Local magnification is an effect seen due to different evaporation fields for different phases within a specimen leading to different trajectories from the tip to the detector, as seen in Figure 1.1 [5]. Since the element evaporation fields are different in these regions, one of the elements is going to want to evaporate at a faster rate while the other is going to require more field strength for the evaporation to occur. Most reconstructions will assume a constant evaporation field and rate, which is not physically the case. Consequently, between these two evaporating materials, a density variation develops within the reconstruction and therefore, the fidelity of the data is lowered [5].

Lawrence *et al.* proposed altering the orientation of the specimen geometry in order to decrease the propensity of fracture failures in semiconductor materials by orienting interfaces between the two very different materials to evaporate simultaneously [6]. This simultaneous evaporation will generate its own set of reconstruction issues because of local magnification and density variations. This work is performed to systematically document the effects of these reconstruction issues as a function of evaporation orientation [6]. For a multilayer thin film, the traditional geometry is shown in Figure 1.2(a). When the evaporation experiment commences for a specimen such as this one, one layer will field evaporate, then the next, and this will continue sequentially. At the interface of the two materials within the specimen, if there exists a difference in elemental evaporation field, there will be preferential evaporation, and the stress builds-up and can produce fractures, as well as reconstruction issues, such as local magnification effects. By changing the orientation of the specimen to that shown in Figure 1.2(b), the proposed idea is that both of the materials will evaporate simultaneously.

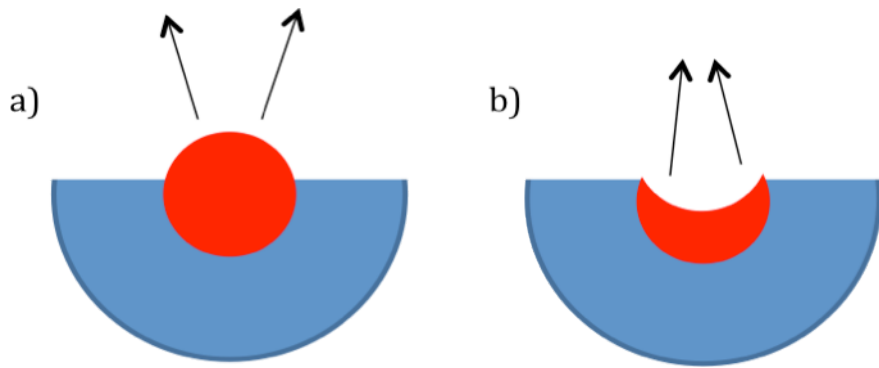


Figure 1.1 Preferential Evaporation due to Different Evaporation Fields
a) Red precipitate has a higher evaporation field
b) Red precipitate has a lower evaporation field

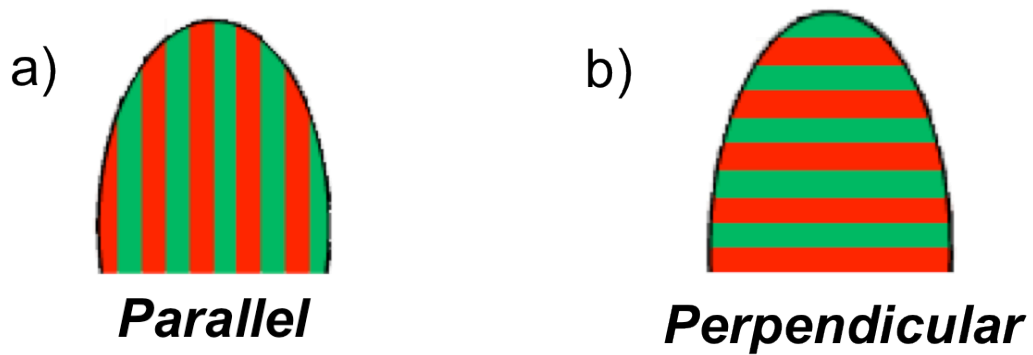


Figure 1.2 Atom Probe Tomography Limiting Geometries

To date, there has not been a self-contained study comparing these two evaporation orientations as a function of materials selection and reconstruction constraints. The motivation for this research was to determine if changing the orientation of the interfaces within a specimen would alter the severity and occurrence of these reconstruction artifacts. In order to perform this in a systematic study, two different sets of materials were manufactured: the first of these contained two elements with very similar elemental evaporation fields and the second contained two elements with vastly different elemental evaporation fields.

In order to be able to confidently identify the fidelity of potential reconstructions, cross-correlation microscopy was employed to quantify the actual composition at the interface between the layers. Cross-correlation has been used to validate atom probe data, including precipitate shape, volume fraction, and chemical composition [7, 8]. In this research, the goal was to identify the local magnification effects and preferential evaporation at the interfaces. The most ideal technique to compare the chemical make-up through the interface to that reported by atom probe was Electron Energy Loss Spectroscopy (EELS). EELS, performed in an aberration-corrected 300 keV Transmission Electron Microscope (TEM), allowed for the collection of the compositional data as a function of distance with nearly sub-nanometer resolution. These collected compositional data sets were used as a reference for the atom probe data in order to identify and quantify the observed reconstruction artifacts.

In the current work, the effect of these reconstruction artifacts found at the interface was quantified for two different cases. Case one looked at two species with similar evaporation field strengths across the elemental interface (iron and nickel with elemental evaporation fields of 33 V/nm and 35 V/nm, respectively), and case two looked at two different species with significantly different evaporation field strengths across the interface (titanium and niobium with elemental

evaporation fields of 28 V/nm and 37 V/nm, respectively) [9]. In addition, the effect of different geometric interface orientations for field evaporation was analyzed. Multilayer thin films, in particular, can be utilized to provide ideal specimen geometries in which to measure and quantify these artifacts generated from field evaporation experiments [7, 10, 11]. Thin films can be deposited with near atomic layer precision and can exhibit large planar surfaces or interfaces featuring a variety of phases and degrees of intermixing. In addition to this, the choice of the layered materials can be tailored to fit different evaporation field strengths across the layered interface.

1.2 Multilayered thin films

The control of nano-scale interdiffusion reactions plays a decisive role for the application of thin films. The interface between phases is often a feature of interest since it can control phase stability, deformation behavior, and chemical segregation and/or reactions [10]. Consequently, the ability to characterize these interfaces is critical to understanding material properties. Atom probe tomography (APT) is uniquely capable of atomic scale chemical measurements with high spatial resolution of such interfaces within the sub-surface of a material [1]. The fidelity of the atom probe data is essential in using it as a technique to qualify interfacial science phenomenon.

1.3 Application of APT in thin films

In modern technological applications, thin films are used for solar cells, optical devices, transistors, and magnetic hard drives, to name a few. As devices and products are driven smaller by size and weight constraints, these thin films are being used in more common applications and

on a more nano-scale. Hono *et al.* investigated Co-Cr thin films in 1992 due to their strong perpendicular magnetic anisotropy. From their research, it was determined that Co-Cr could be a promising candidate for perpendicular recording media [12]. In order to determine the feasibility of this material system in this particular application, understanding the fundamental nature of the microstructure was of great importance [12]. In order to perform this nano-scale analysis of the deposited thin films, field ion microscopy and atom probe tomography were both implemented to quantify the fluctuations in concentration within the bulk of the sample.

Teng *et al.* worked on characterizing the magnetization behavior of TbFeCo thin film materials as a function of the chemical composition. This particular system was of interest because of its unique perpendicular magnetization characteristics and how that applies to magneto-optical recording media [13]. Then, they examined the magnetic coupling phenomenon that occurs between the TbFeCo thin films. In 2007, Feng *et al.* also characterized magnetic materials for the application of high-density magnetic recording. The specimens used in this research, however, were comprised of SmCo/Cr/TbFeCo and varied by thickness variations of the Cr interlayer [14].

Vovk *et al.* studied the reactive interdiffusion of Co-Al bilayers. This was done because the development of nano-technologies defines the advance of modern electronic devices. The earliest stages of interdiffusion in these devices are of particular interest in determining their capability in application [15]. By the use of APT, the specific quantification of diffusion at different time scales was observed. The high driving forces present in such small devices allows for non-equilibrium stages to appear, mostly solid state amorphization in multilayered diffusion couples. The earliest stages of this reaction are denoted by steep compositional gradients within the fabricated device [15].

Thompson *et al.* used atom probe tomography to characterize the compositional gradient present in SiGe structures as they are used in nano-devices [16]. This research was performed to analyze the capabilities and limitations of techniques used for compositional analysis. As the feature length scales in nano-devices shrinks below 10 nm, the variations in the chemical composition, specifically the location of dopant atoms and the integrity of the planar interfaces between regions, may have a significant impact on the final electrical characteristics of the device [16]. As a result of this, it is important to characterize the chemical composition of these nanostructures as close to the atomic level as possible.

1.4 Development of APT

Over the past decade, atom probe tomography (APT) has undergone major improvements, which not only dramatically improve the performance of three-dimensional atom probes, but also extends the range of materials that can be characterized utilizing these tools [5]. The improvements within the instrumentation include a large field-of-view and data collection rates while providing a higher mass resolution. The recent integration of reliable, high repetition rate femtosecond pulsed lasers allows field evaporation to be assisted by laser pulsing for specimens that have a low electrical conductivity. These materials include semiconductors and ceramics [5]. Simply, the atom probe can be conceived as a field ion microscope (FIM) with an attached time-of-flight mass spectrometer, allowing chemical characterization of individual surface atoms.

In field ion microscopy, a sharp cryogenically-cooled needle-shaped specimen is pointed at a phosphorous screen. A trace amount of image gas, typically neon or helium, is introduced into the ultra-high vacuum system with a base pressure less than 2×10^{-8} Pa. A positive voltage

is then applied across the surface of the specimen, resulting in an electrical field at the apex of the specimen tip. Nearby image-gas atoms become polarized and are attracted to the specimen surface where they are thermally accommodated. When the field reaches a critical value, these image-gas atoms are field ionized close to the surface. The resulting atoms are repelled towards the screen where they form the field ion image. As the rate of ionization is highest over the nuclei of the most protruding surface atoms, this image can be used as a map displaying the position of these atoms. As this field is increased, specimen surface atoms are expelled from the specimen as ions. This removal process is what is known as “field evaporation” [5]. Field evaporation enables the interior of the prepared specimen to be analyzed.

The first generation of atom probe field ion microscopes (APFIM), initiated by Müller, Panitz, and McClane in the late 1960s featured a 1-2 mm circular aperture in the field ion detector that worked as the entrance to the time-of-flight mass spectrometer [17]. In this instrument, atoms were evaporated by pulsing an increased voltage from a static electric field that was implemented on the surface of the specimen. This allowed for the production of a narrow circular cross-sectional volume that typically contained up to 50,000 collected atoms [17]. In 1982, Kellogg and Tsong developed an alternative method for field evaporating ions from a prepared specimen. This new method involved pulsing a laser in order to provide the atoms with enough energy to be expelled from the surface [18]. Laser pulsing, however, did not immediately gain acceptance for metallurgical applications due to the unreliable nature of the lasers available at the time.

The second generation of atom probe instruments, first introduced in the late 1980s, used a variety of position-sensitive single atom detectors [19]. This three-dimensional approach to imaging increased the lateral field-of-view of the specimen from the 1-2 mm allowed by the first

generation to 10-20 mm. This volumetric expansion allowed for the data sets to enter millions of collected ions. In both the first and second generation atom probe instruments, field ion microscopy had to be performed at the start of the experiment in order to align the specimen with the entrance to the mass spectrometer as well as to select the most ideal initial area of interest for the experiment.

The most recent generation of atom probe instruments includes the local electrode atom probe (LEAP®), introduced by Kelly et al in 2003 [20]. This design features a local electrode in close proximity to the specimen, as shown in Figure 1.3. The main advantages of this local electrode are the ability to work with a lower-amplitude standing and pulsing voltages, and it also increases the detector's field-of-view. Having a lower pulse amplitude allowed the use of voltage pulse generators with much higher pulse repetition rates, up to 200 kHz. In order to accommodate these improvements, the LEAP also used faster delay line single atom detectors. Local electrodes require that the apex of the specimen be aligned precisely with the central aperture in the local electrode. Due to the requirements for an extra set of three specimen translations and increased specimen positional stability with respect to the local electrode, coupled with the wide field-of-view of the detector, the ability to rotate the specimen to select a position on the surface was not incorporated into this design [20]. This averted the need to perform field ion microscopy at the start of the experiment.

During the measurement, the evaporation rate is usually kept constant, controlled by the voltage at the apex of the specimen [21]. If, in the specimen geometry, a layer of high evaporation field strength is deposited on top of a material of lower field strength, the measurements enters an unstable situation when the interface between these two phases is reached during the evaporation experiment. As soon as the easily evaporating material becomes

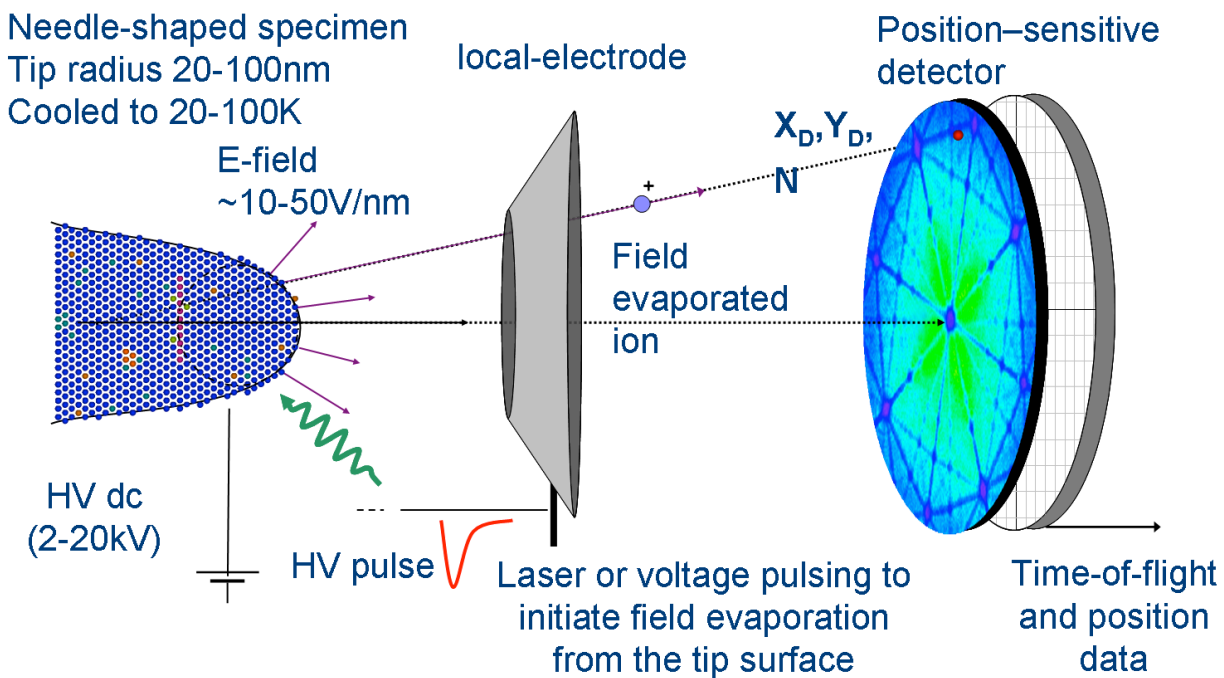


Figure 1.3 Local Electrode Atom Probe® Schematic [21]

uncovered, the rate at which atoms are field evaporated increases dramatically. In most cases, this cannot be compensated by a quick reduction of the tip voltage, resulting in a specimen fracture [22].

In order to obtain a reliable reconstruction of the atomic positions within the specimen, it is advantageous to keep the evaporation rate homogeneous along the specimen surface during the field evaporation experiment. Schmitz proposed in 2003 that this requirement is best achieved if there is a careful pre-development of the substrates, which shapes the tip to obtain an iso-field surface [22]. Therefore, in this proposed experiment, a new layer with different evaporation properties becomes completely uncovered at once, maintaining a constant iso-field surface across the tip.

When the evaporation field strength between two materials is sufficiently different, the specimen can fracture under field evaporation. In general, this occurs because the atom probe instrument is attempting to adjust the required voltage to meet the field evaporation strength for each material present at the interface. [23]. This voltage adjustment can generate considerable amounts of mechanical stress on the tip. In particular to multilayers, evaporating with the layers normal to the evaporation direction, can result in fracture as you transition from one layer into a different layer.

Lawrence *et al.* [6] reported that by altering the orientation of the thin film interfaces to be parallel to the evaporation direction reduced the propensity of ‘fracture type failures’ because of simultaneous evaporation of each layer, as shown in Figure 1.2(b). When the chemical modulations are perpendicular to the evaporation direction, the evaporation progresses layer-by-layer; in contrast, when the chemical modulations are parallel to the evaporation direction, simultaneous evaporation occurs for each layer. To date, little work has been reported on

comparing the reconstruction differences of evaporating specimens in each orientation and how the relative field strengths between the layers influences the reconstruction in each comparative orientation. In modern atom probe instruments, the maximum spatial resolution in the xy-plane is 0.5 nm while the maximum spatial resolution in the z-direction is 0.05 nm [23]. By orienting the interfaces parallel to the evaporation direction, the proposed concept is that the generation and effects of artifacts will be decreased, but in doing so, the spatial resolution within the interfaces is sacrificed by approximately an order of magnitude. Performing this systematic study will show whether the artifacts are diminished by changing the orientation and whether this loss in spatial resolution is worth the advantages.

The basic information produced by the atom probe is a sequence of the atomic coordinates and the mass-to-charge state of each ion collected [5]. After the completion of the experiment, these data are typically reconstructed into a digital three-dimensional representation of the volume analyzed. This reconstructed data can be characterized in order to obtain information about the solute distribution within the microstructure. The resulting reconstructed volume is a truncated cone in which the radius increases during the experiment in relation to the shank angle of the needle-shaped specimen [5]. In the most modern versions of these instruments, the data sets can contain typically millions of collected ions.

Within these reconstructed data sets, the lateral atomic coordinates, x and y, are derived from the positions of the impact of each ion on the position-sensitive detector, X and Y. For example, the atomic coordinates of each ion are given to a first approximation by $x=X/\eta$ and $y=Y/\eta$ where the magnification, η , is given to a first approximation by $\eta=d/\xi r$, where d is the specimen-to-detector distance, ξ is a projection parameter known as the image compression factor, and r is the radius of curvature [5]. The radius r generally increases during the

experiment and is given by $r=V/\kappa F$, where F is the evaporation field at the specimen apex and κ is a geometrical factor.

The mass-to-charge state is estimated from the potential energy neV of the escaping ion, where V is the applied voltage between the specimen and the local electrode that is the entrance aperture to the mass spectrometer. At this entrance, the kinetic energy is $\frac{1}{2} mv^2$. The ion velocity, v , can be estimated from the distance from the specimen to the single atom detector, d , and the flight time, t . The overall result of this is

$$\frac{m}{n} = \frac{C * (V_{dc} + \alpha V_{pulse}) * t^2}{d^2} \quad 1.1$$

where V_{dc} and V_{pulse} are the standing and pulse voltages applied to the specimen, α is the pulse amplitude coupling factor to account for some loss in the effectiveness of the pulse, and c is a constant ($c=1.93 \times 10^{-4}$) used to convert the mass into atomic mass units, amu [5]. The typical detection efficiency of the three-dimensional atom probe is approximately 50-60% of all the ions removed from the specimen.

1.5 Atom probe reconstruction

The distribution of atoms within a reconstructed atom map may be visualized as a three-dimensional map of color-coded spheres, signifying each atom of interest at its magnified coordinates. When the data has been collected from an instrument with a wide field-of-view, the extent of the data may be too large to clearly distinguish any of the features of interest due to a large number of atoms. In this case, selected regions of interest are extracted from the collected spectrum [5]. Phases, clusters, segregation to microstructural features, such as dislocations, interfaces, and grain boundaries, may be deduced from local solute enrichments. In actuality, the local density of atoms is a combination of the solute concentration and the atomic density of the

phases. Other factors, such as local magnification effects because of differences in evaporation fields for different elements, trajectory aberrations at the emergence of major poles and zone lines on the surface can lead to variations in the observed density of atoms [24]. Because of this, careful quantification and reconstruction is required when interpreting solute enrichments or interdiffusion across phase or grain boundaries.

The morphology and size of phases within a reconstructed atom map may be graphically visualized utilizing isoconcentration surfaces. In this representation, the three-dimensional data is divided into small cubes, known as voxels, typically containing 20 to 100 atoms. The concentration of one or more selected elements of interest is then determined for each voxel. The surface for a particular concentration over the entire three-dimensional volume may then be constructed. Although the inner and outer surfaces may be apparent from the color-coded spheres, an atom map may be superimposed on the isoconcentration surface to more clearly distinguish the two phases present in the specimen. A concentration profile may then be calculated across the interface or grain boundary. To do this, the volume is further subdivided into thin slices perpendicular to the interface and the composition of each slice is determined and plotted as a function of distance along the major axis [5]. More commonly, when implementing an isoconcentration surface, the solute distribution across an interphase interface may be determined with the proximity histogram, also known as a proxigram, developed by Hellman *et al.* [25].

Hellman *et al.* developed this method because it provides the unique advantage of allowing accommodation of the curvature of non-planar interfaces and requires significantly less user interaction [25]. In this method, an isoconcentration surface is constructed, then the shortest distance of each atom to the nearest isoconcentration is determined and the identity of the solute

atom is accumulated into a data bin at that distance from the interface. The solute concentration is then plotted as a function of distance from the isoconcentration surface. Further, proximity histograms from multiple interfaces in the same volume of interest may be combined in order to reduce the statistical sampling error [25].

1.6 Electron Energy Loss Spectroscopy

Compositional analysis based on characteristic x-ray excitation faces two practical problems. The first of these is the very low collection efficiency of x-rays (10^{-3} for wavelength dispersive spectroscopy and 10^{-2} for energy dispersive spectroscopy). The second problem is the inefficient characteristic x-ray excitation and the poor detection resolution or radiation generated from the light elements. Although the characteristic spectra from the elements below magnesium are readily detectable down to lithium, these elements are difficult to analyze quantitatively due to absorption issues [26].

Analysis of the energy spectrum of the inelastically forward scattered electrons, overcomes these limitations in EDS and WDS devices due to very high collection efficiencies—over 50% possible while maximum sensitivity is achieved for the low energy losses that are characteristic of the low atomic number elements. The electron energy loss spectrum is also usually measured by thin film transmission microscopy, using forward scattered electrons. This angle of scatter is the most difficult for x-ray microanalysis due to the poor counting statistics. Due to the shortcomings of the EDS and WDS techniques for spatial compositions, EELS was used as the other technique for cross-correlation microscopy. EELS allows for the collection of nano-scale compositional data as a function of distance across the specimen. Two primary modes of operation are possible for EELS in the conventional transmission electron microscope.

If an image is focused on the phosphorus screen, then the back focal plane of the projector lens will contain a diffraction pattern that can serve as the signal for an EELS spectrometer. The selected area aperture in this plane determines the origin of the signal and the image formed in the back focal plane of the projector lens is the image observed within the spectrometer.

Alternatively, if a diffraction pattern is focused on the screen, then the back focal plane contains an image that serves as the signal source for the EELS spectrometer, and the source of the signal is then the area of the specimen within the selected area aperture that is illuminated by the incident beam. Focusing the incident beam, to form a convergent beam diffraction pattern on the viewing screen, can also be used to define the region from which an EELS signal is acquired [7].

If the incident electron beam is fully focused to a fine probe, as in scanning transmission electron microscopy (STEM), then this will be analogous to a diffraction pattern that is focused on the viewing screen. The STEM probe will then also define the sample area from which the signal is collected. In effect, it is the electrons focused in the back focal plane of the microscope that determines the source of the EELS spectrum [26]. The advantage of STEM mode is that the electron beam can be rastered across the sample, to acquire EELS data as a function of the position of the incident electron probe, in order to form an EELS line-scan or composition map. Additionally, when using a field emission gun source, the spatial resolution of the EELS signal is actually better in STEM mode than it is in TEM mode, and sub-nanometer spatial resolution of EELS results for chemical compositions have been demonstrated.

The electron energy loss spectrometer is a magnetic prism positioned beneath the main column of the microscope, as shown in Figure 1.4. The magnetic spectrometer is located below the primary image plane of the microscope and accepts electrons that pass through an aperture

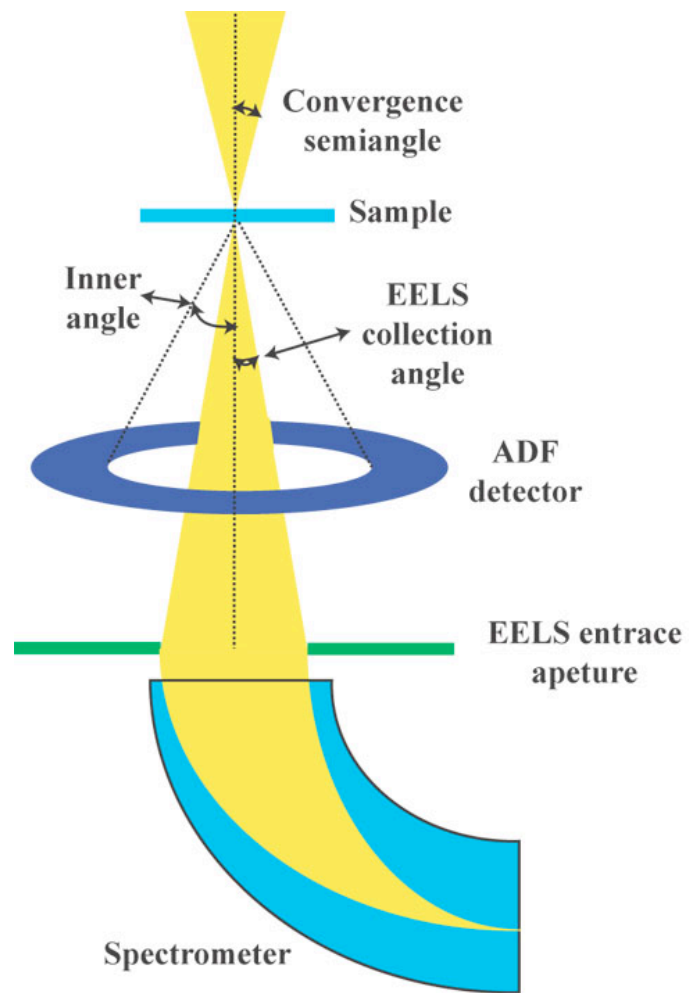


Figure 1.4 Electron Energy Loss Spectroscopy Schematic [27]

positioned on the optic axis. The electrons deflected by the spectrometer will have an angular spread, with those electrons of energy E_0 that have experienced no energy loss being the least deflected. All electrons that have experienced an energy loss will be deflected by an additional angle that is dependent on the extent of energy loss [26].

1.7 Electron Energy Loss Spectrum

A typical energy loss spectrum is shown in Figure 1.5. The y-axis is the detected intensity at a given energy, measured in arbitrary units. The x-axis is the energy loss ($E_0 - E$), measured in eV. Energy losses as high as 2000 eV can be detected, but the count rates at high-energy losses are very low. The high-energy loss region of the spectrum ($\Delta E > 50$ eV) contains the inner shell absorption edges that are associated with atomic ionization and are accessible for chemical analysis in EELS. Because the spectral resolution in EELS is so much better than that available for EDS or WDS, more detailed information is available in the excitation edge associated with each individual atomic species. Moreover, since EELS is particularly sensitive to low energy excitations, this signal contains considerable chemical information [26].

In order to collect information at the optimal resolution of the tool, around 0.1 eV, a monochromatic field emission source is required. In most cases, it is the kinetic energy involved in the spread of the beam, not the characteristics of the EELS detector, which limit the energy resolution. Therefore, it is common practice to record the zero-loss peak, corresponding to the primary Gaussian peak for the beam exiting the specimen to calibrate both the absolute zero for the energy loss spectrum and to estimate the available energy resolution, usually from the full-width-half-maximum of the zero-loss peak. Fitting an empirical function to the pre-edge data and then extrapolating the estimated background curve to the high-energy loss region can only

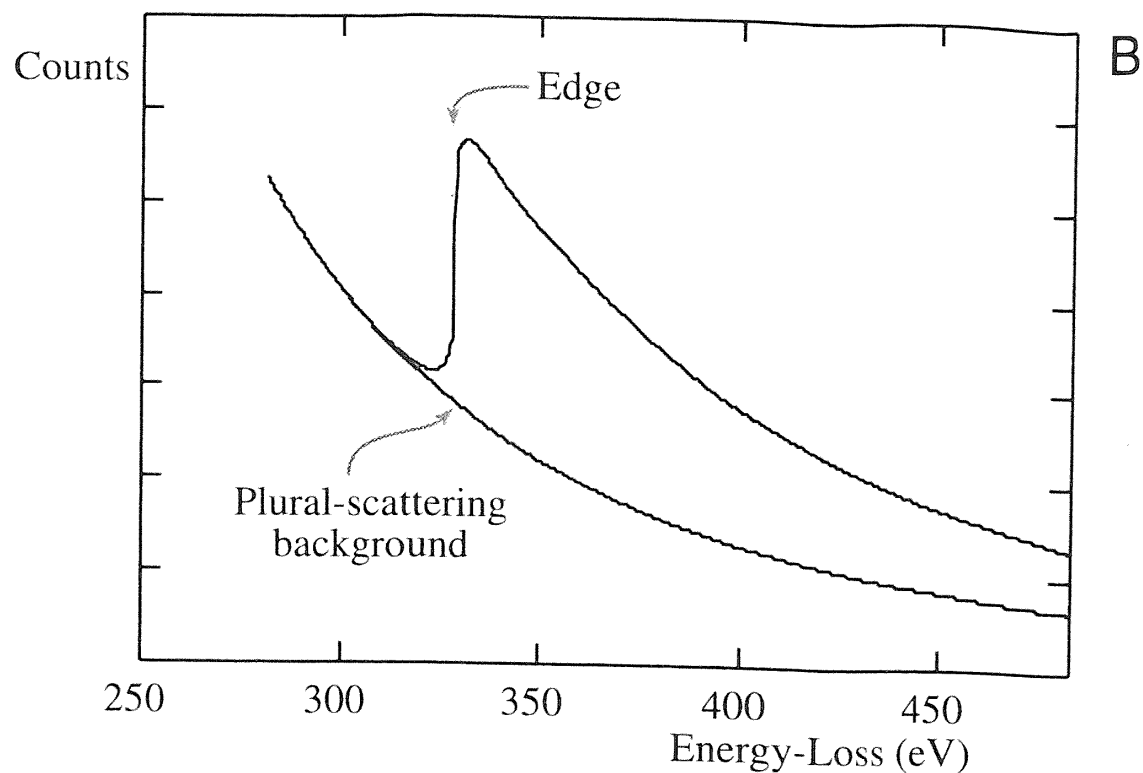


Figure 1.5 Typical EELS Energy Loss Spectrum [28]

estimate the total number of events associated with any particular absorption edge. The estimated background is then subtracted from the measured data to yield a value for the true number of absorption events.

The signal from each edge decreases rapidly at higher energy loss values and it is not necessary to sum the counts derived for a particular edge over all energies above that edge. However, it is important that the data for all edges should be summed over the same range of energy loss. This energy loss window is typically 50-100 eV, and the same window can be used to derive an absolute mass data scale by applying this window to the zero-loss and low energy plasmon loss region. The assumption is that the data are collected over a fixed solid angle, the collection semi-angle, β determined by the spectrometer aperture, and that the inelastic scattering cross-section for this solid angle and energy range is known, so that good estimated values for K excitation are assumed to be available. Characteristic x-ray microanalysis, using EDS or WDS methods, remains far more accurate for quantitative microanalysis, but they cannot compete with EELS in mass sensitivity. EELS methods, however, have far better spatial resolution and detection limits, making it a more viable option for near atomic-scale compositional profiles. [26].

CHAPTER 2

EXPERIMENTAL

2.1 Sputter deposition

The Fe/Ni and Ti/Nb elementally layered thin films were deposited in the AJA ATC-1500 stainless steel magnetron-sputtering chamber shown in Figure 2.1. The chamber is evacuated to a base pressure of 1×10^{-8} Torr by a mechanical and turbo-molecular pump. A load lock was used in order to insert and retrieve samples without disturbing the base pressure of the main chamber. All of the films were sputter deposited at ambient temperature onto 5 cm, p-type boron doped, low resistivity Si [100] wafers. In order to insure uniform film growth, the substrate was rotated at about 20 revolutions per minute at a height of about 100 mm from the surface of the elemental targets to ensure +/-2% thickness uniformity. The total film thickness was $\sim 1 \mu\text{m}$ with a chemical modulation or bilayer of $\sim 4 \text{ nm}$ with each layer being of approximate equal thickness. This sputtering chamber contains four con-focal magnetron sputtering guns with pneumatically operated shutters over each target. Ultra-high purity argon gas was used as the working gas during sputtering at a pressure of 2.0 mTorr at a flow rate of 10 standard cubic centimeters per minute.

In order to provide reproducible layers within a film, a Labview® program was implemented to provide a programmable user interface that would control each gun shutter and sputtering power during the deposition process. Before beginning deposition, the user inputs the desired gun's location in the chamber, gun power, and deposition time, as seen in Figure 2.2. This program allows for a constant or variable power each individual sputtering gun



Figure 2.1 AJA ATC-1500 Stainless Steel Magnetron Sputtering System



Figure 2.2 LABVIEW® User System Interface

allowing precise control of the deposition rate at any time during the growth of the thin films in order to have repeatable, identical layers.

In order to design an experiment that would allow for a quick and easy cross correlation between the atom probe and EELS techniques, the films were deposited with each element having a sputtered layer thickness of about 2 nm. Precise deposition rates as a function of sputtering power for the four different elements: Fe, Ni, Ti, and Nb were determined using X-ray Reflectivity (XRR) [29, 30]. Based on the thickness of the elemental targets and the voltage applied through the sputtering gun, an approximate sputtering rate was determined based on previous experiments performed using the same sputtering chamber. A purely elemental film was then deposited for each of the four elements in this study at a target thickness of 50 nm. These films were analyzed in a Phillips XPERT X-ray Diffractometer (XRD) using the typical operating conditions for XRR. Based on the spacing of the peaks within this pattern, the actual thickness of each of the films could be calculated. Dividing this thickness value by the amount of time the sputtering guns were operational gave the effective deposition rate to be used for creating the samples.

2.2 Analytical Instruments

2.2.1 FIB Overview—TEM foil preparation

Cross-sectional Transmission Electron Microscopy (TEM) samples were prepared using an FEI Quanta 3D Dual-Beam Focused Ion Beam – Scanning Electron Microscope (FIB-SEM). The FEI Dual-Beam's capabilities include a 5-30 keV tungsten filament electron beam source and a 5-30 keV gallium liquid metal ion source (LMIS) positioned at an angle of 52° from the electron beam, as shown in Figure 2.3. The FIB allows for sight specific sample preparation

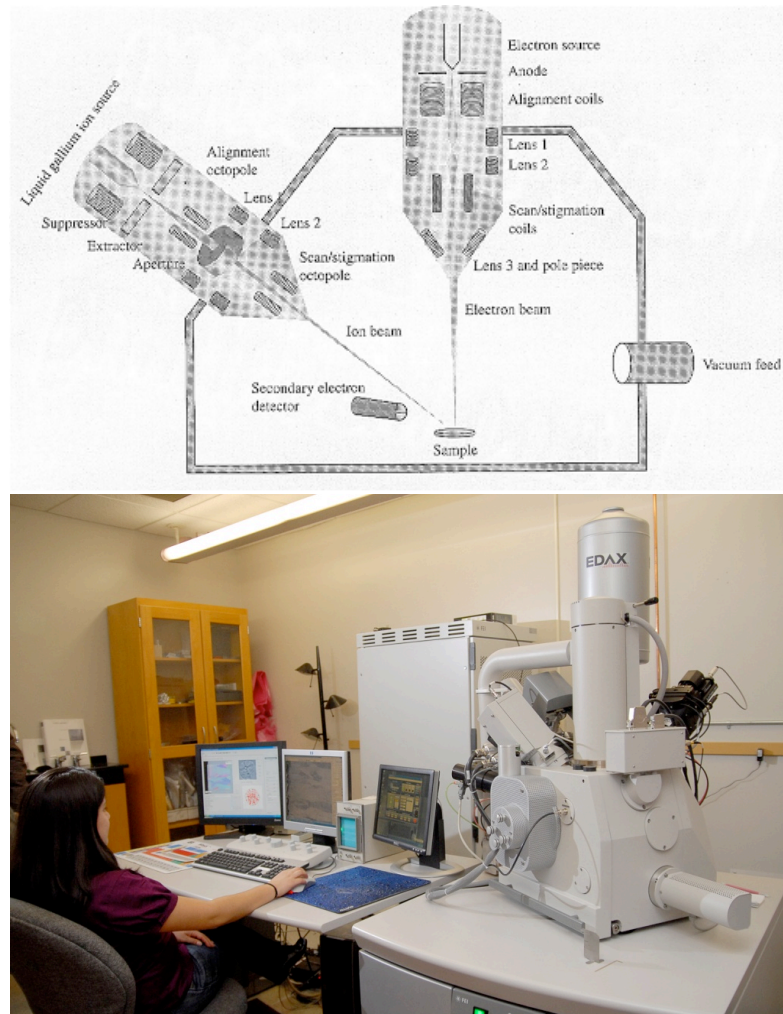


Figure 2.3 Schematic of FEI Quanta 3D Dual Beam FIB [31]

and extraction. Cross-sectional TEM samples were specifically chosen due to their orientation in the microscope. When viewing cross-sectional TEM samples, the image is created in an edge-on fashion to the layer interfaces. This allows the EELS profiles to be collected as the beam scans through one layer, through the interface, and into the next layer. Not only can the thickness of each of the layers be quantified, but also, the amount of intermixing occurring at the interfaces can be quantified as a compositional gradient. This is the best orientation for comparison to the APT compositional profiles.

The samples were milled-out and thinned using a run-script program provided by FEI. This program cuts a cross sectional sample followed by manual FIB thinning. The steps of the TEM preparation are shown step-by-step in Figure 2.4 [32]. The thin foils were then removed from the bulk of the sample utilizing an ex-situ manipulator and placed on a copper Omniprobe® grid. The attachment to this grid is completed utilizing the in-situ Gas Injection System (GIS) Pt deposition inside the FIB. The GIS flows a Pt-based organic gas over the sample which breaks down under either the ion or the electron beam. A Pt film, serving as a ‘weld’ between the sample and the grid, is built up over time and holds the sample onto the grid.

Since these samples were to be used in high resolution STEM-EELS, an additional ex-situ ion milling procedure was utilized. The process of FIB lift-out can induce surface damage during its milling [33]. In order to remove this damaged layer, the sample is placed into a Gatan Precision Ion Polishing System (PIPS) where it is bombarded with low energy Ar⁺ ions. The PIPS has two rotatable ion guns with a beam voltage range of 1-5 keV. The ion guns can be rotated to mill the top or bottom of the sample. Polishing with the PIPS was performed

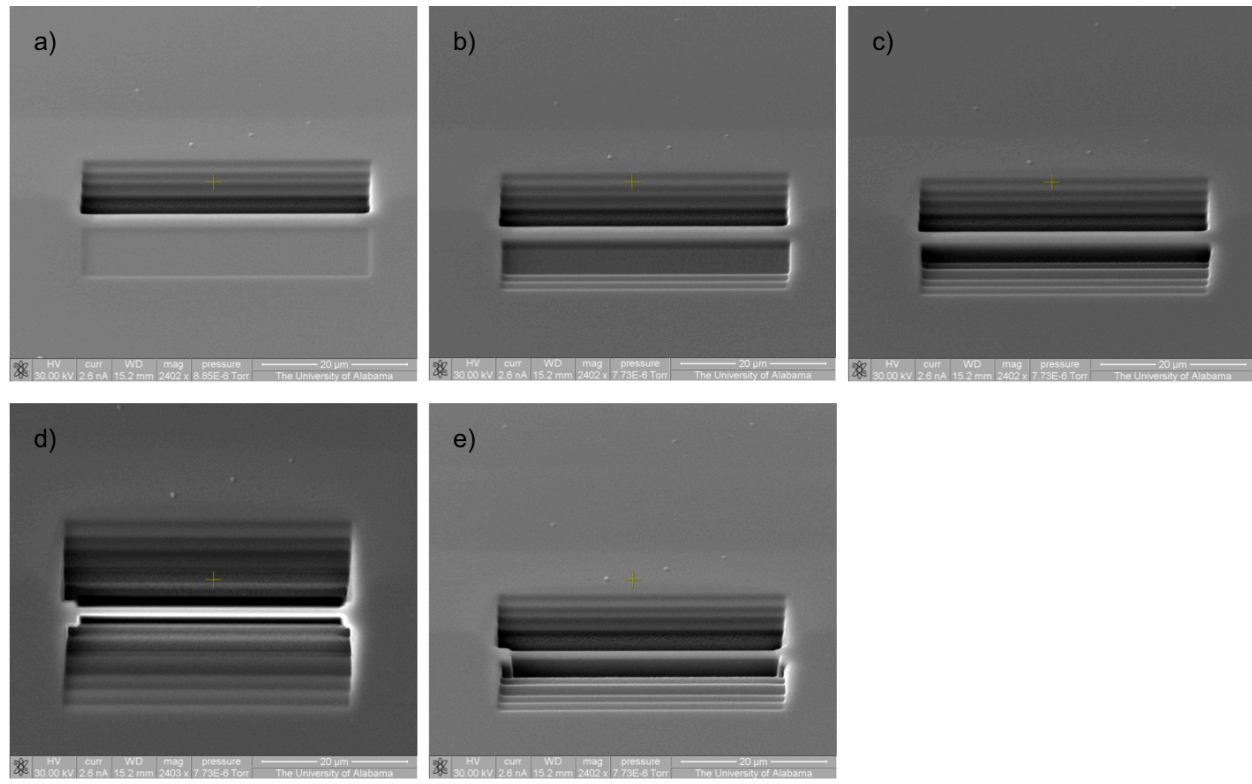


Figure 2.4 Schematic of TEM Foil Lift-Out Procedure

according to the specifications recommended by the owner's manual: 6° on the top and bottom with an accelerating voltage of 2 keV.

2.2.2 TEM Phase ID

Plan-view selected area electron diffraction provided the means for phase identification of the deposited thin films since it allows the user to look through the 'bulk' of the material using a TEM. The d-spacing value associated with each the {hkl} diffraction rings was calculated by measuring the projected radius of the ring and applying it into Equation 2.1 [33]:

$$dR = \lambda L \quad 2.1$$

where d is the lattice spacing for the diffracted {hkl} plane, R is the measured radial projection of the ring, λ is the electron wavelength, and L is the camera length.

These TEM foils were prepared by a process that involves sectioning a 3 mm disc from the sputter deposited film and then thinning to electron transparency using a sequential process of grinding, dimple grinding the middle of the disc, and implementing an ion mill in order to cause perforation from the substrate side of the sample (film deposited on silicon substrate). Along this perforated region, there are electron transparent regions of the film that were analyzed using a FEI Tecnai TEM operated at 200keV.

2.2.3 STEM-EELS Analysis

The TEM foils lifted-out using the FIB-SEM were characterized in a 300 keV aberration corrected FEI Titan TEM located at the National Institute of Standards and Technology (NIST). This EELS portion of the research was performed under the direction and expertise of Dr. Andrew Herzing and Dr. Ian Anderson. Both bright field and high angle annular dark field

(HAADF) images were used to verify the bilayer thickness. To ensure no projection issues, the Si substrate portion of the foil was tilted down the [010] zone axis; therefore, the beam was normal to the cross-sectioned multilayer viewing direction. The EELS data was collected in this orientation with a pixel size of 50 pm and an energy resolution of 0.5 eV/ch. The Fe L (708 eV) and the Ni L (855 eV) as well as the Ti L (456 eV) and the Nb M (205 eV) energy edges were used to produce the spectrum for the Fe/Ni and Ti/Nb multilayers, respectively. The resulting background was subtracted from the energy edge by using the pre-edge window power-law extrapolation model. In the case of the Fe L edge, a 60 eV window was used. The computed background model was then subtracted from every spectrum in the data-cube, resulting in the formed sum spectrum, shown in Figure 2.5. The background for the Ni edge is removed in a similar fashion, but it is important to realize that the background in this case originates from the normal spectral background and the residual intensity from the Fe edge.

The composition of the EELS spectrum was determined using the following procedure: By integrating the signal within the energy-selection window in each pixel of the data cube, these intensities were plotted against the spatial positions to extract the edge profiles. The composition profiles where then calculated by applying a correction-factor which relates the edge-intensity to the number of atoms in the specimen, and this factor is the partial ionization cross section for this specimen. To compute the composition profiles in this case, the theoretical Hartree-Slater values for the Fe L edge and the Ni L edge were used. These values are contained in a database within Gatan Digital Micrograph and are analogous to the Cliff-Lorimer (k-factor) corrections used in quantitative energy dispersive spectroscopy analysis [26]. Essentially, the Fe to Ni ratio is calculated by taking the ratio of the products of the cross-section value and the integrated intensity for each element.

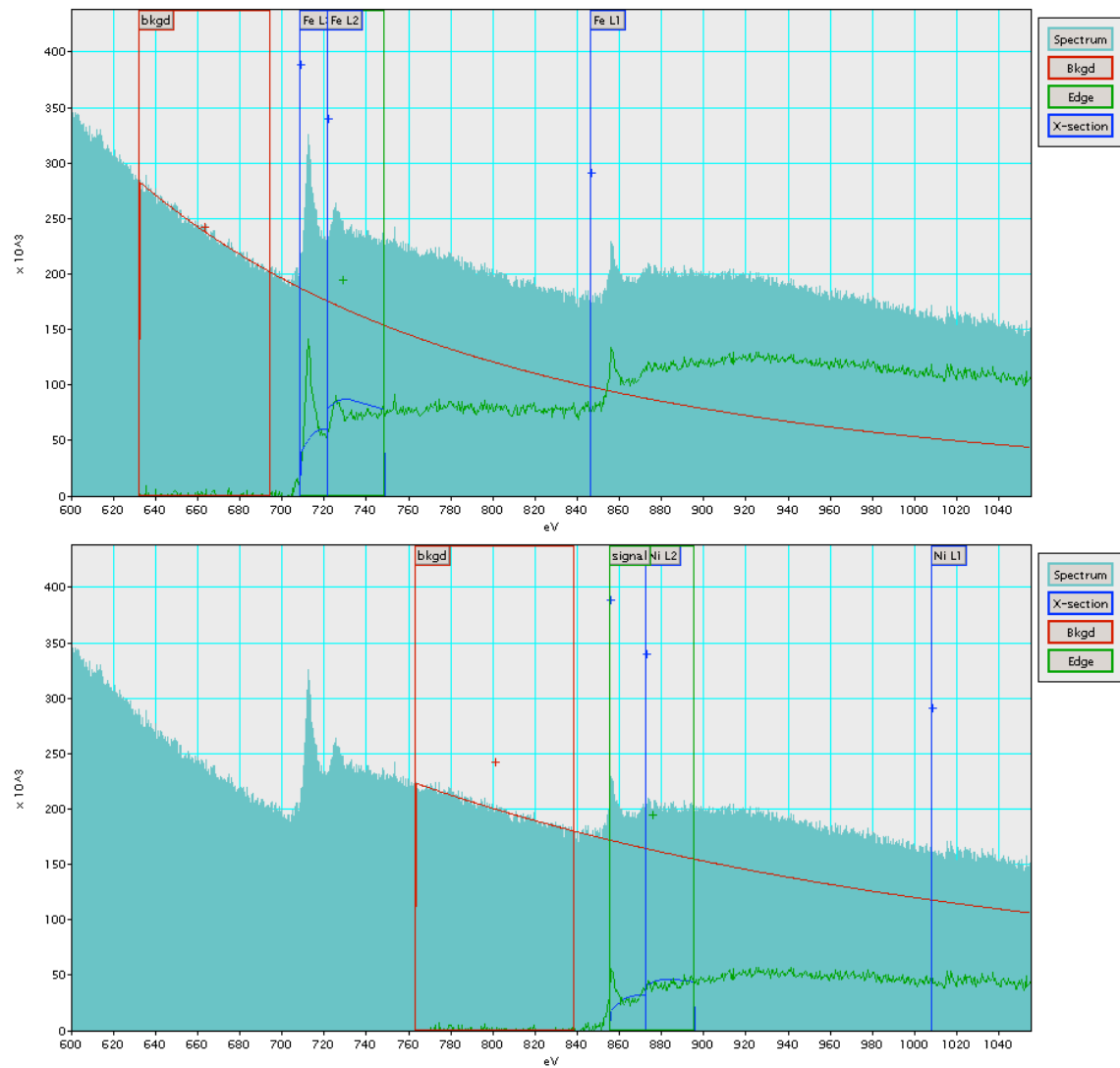


Figure 2.5 EELS Spectrum for the Fe/Ni ~4 nm Bilayer Film

This method was similarly applied to the data acquired from the Ti/Nb film in order to output a corrected one-dimensional compositional profile. The main difference between the analysis of the Fe/Ni and the Ti/Nb multilayers is the fact that in the analysis of the latter bilayered film, the M edge is needed for niobium. This is because it has a relatively high atomic number for EELS analysis. The L edge is at too high of an energy to analyze, but the M has a slow onset, unlike the characteristically sharp L edge. This means that instead of the sharp edge seen in Figure 2.5, the niobium M edge has a rounded hump. Due to this ‘slow onset,’ it is very difficult to precisely identify a reference for niobium. Other researchers who have analyzed this system, such as Genc, were able to do so by depositing and characterizing a very thick film so that there were portions of the elemental layers that had pure niobium [7]. By performing EELS on this pure region, an internal standard could be created for reference at the intermixed interfaces. This was not done as the profile shape across the interface, not absolute compositional values, was needed. This shape is independent of the absolute values. Thus for Ti/Nb, the areal density was employed.

In the set of films analyzed in this research, the layer thicknesses were small enough that there were not purely elemental niobium areas that could be analyzed with any degree of certainty. Because of this, a precise composition could not be computed for the Ti/Nb multilayered film. Niobium has not been measured and quantified into a standard for EELS, so without a pure niobium standard within the film, there is no way to convert the scan data into a composition. What can be computed, however, is the number of atoms of each element per area. For the purposes of this study, this data is sufficient since the EELS spectrum is used to identify reconstruction artifacts in the APT technique, and the number of atoms per area can be analyzed similar to a composition as a gradient across an interface.

2.2.4 APT Sample Preparation

A Cameca (formerly Imago Scientific Instruments) Local Electrode Atom Probe (LEAP®) 3000XSi was used in order to field evaporate the atom probe tips, as shown in Figure 2.6. The LEAP, unlike traditional atom probes, have high data acquisition rates and increased field of views (>100 nm) [36]. To allow for reasonable voltages of a few thousand volts and acquire electric field strengths of about 10^{-6} N/m needed for field evaporation, specimens must be prepared to have a needle shape with a radius of curvature of about 100 nm or smaller.

2.2.4.1 Perpendicular APT Specimen Preparation

These APT specimens were traditionally prepared by the *in-situ* removal of a wedge of the film from the substrate as described by Thompson *et al.* [37]. A region of interest is first identified on the surface of the sample by identifying an area with good surface integrity and very little post-deposition debris. A 300 nm thick capping layer of Pt was then deposited onto the surface of this region in order to limit the amount of gallium ion implantation during the cutting and imaging process. This cap was measured to be about 40 μm long by about 2 μm wide. Trench milling was then performed at a cutting angle of 30° around this region. This cut was 45 μm long and about 0.5 μm wide, and it was performed to a depth of about 5 μm . The sample was then compucentrically rotated 180° so that an identical cut could be performed on the opposite side of the Pt protective cap. Finally, the ends of the region of interest were then milled out. This wedge is then extracted from the bulk of the thin film by utilizing an ex-situ manipulator. This process is laid out below in Figure 2.7.



Figure 2.6 Cameca® (Formerly Imago Scientific Instruments) LEAP 3000XSi

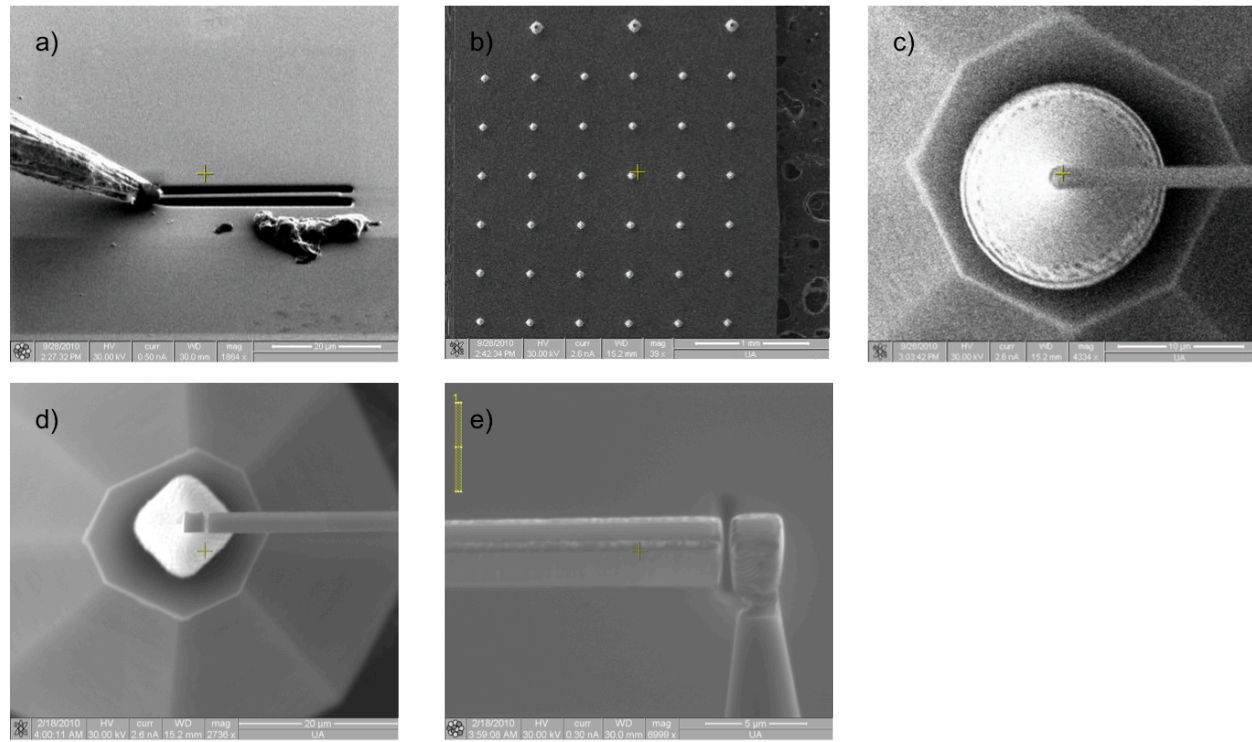


Figure 2.7 APT In-Situ Tip Preparation, Perpendicular Orientation

At this point in the preparation process, the specimen is ready to be adhered to a Si flat-top microtip coupon. The tip at the long end of the sample was lowered onto the tip of the flat top, and the wedge was adhered to it by using the GIS Pt deposition tool within the FIB. Once the wedge was secured to the post, the ion beam was used to slice this welded part off from the rest of the specimen. This was then repeated five more times until six specimens had been created from this one wedge. The microtip coupon was then rotated 180° so that Pt could be deposited onto the other side of the mounted specimens, completing the adhesion process. The mounted specimens were milled into appropriate atom probe specimens by applying a set sequence of annular milling patters in order to thin the specimen into a long needle-like specimen with a tip radius of about 100 nm. A low-keV cleaning mill was then used to remove any gallium ion implantation that may have occurred during the thinning process. This process was in accordance with previously performed research [11, 37].

For multilayered thin films, such as the Fe/Ni and Ti/Nb films used in these experiments, this extraction, mounting, and sharpening process yields specimens, that when used in a field evaporation experiment, will exhibit an evaporation behavior that progress layer-by-layer as the specimen surface moves downward from the apex of the tip. In this orientation, the experiment will continue downwards, perpendicular to the interface between the two layers. This is known as the perpendicular geometry, as shown in Figure 1.2(a). In contrast to this specimen orientation, the parallel geometry, shown in Figure 1.2(b) shows an atom probe tip that would field evaporate all of the deposited layers at the same time, as proposed and outlined by Lawrence *et al.* [6].

2.2.4.2 Parallel APT Specimen Preparation

In order to prepare the atom probe samples that would be oriented in an edge-on fashion, the steps layed out by the research performed by Lawrence *et al.* [6] were adhered to in order to generate the most ideal specimens. A step-by-step procedure of this lift-out process is shown in Figure 2.8. The film was first cleaved and mounted vertically within the chamber of the FIB-SEM. A region on the film edge of the sample was chosen to be the region of interest. A 300 nm thick platinum cap was deposited at this point. It measured approximately 40 μm long by about 2 μm thick. Much like in the original orientation, a 30° trench mill was performed on the silicon side of the cap. However, in this case, the cut was only performed on one side in order to preserve the integrity of the film. The *ex-situ* manipulator was then attached to this triangular wedge, and the ends were milled away so that it can be lifted out.

At this point in the preparation process, the sample is ready to be adhered to a silicon flat top microtip coupon. The tip at the long end of the sample was lowered onto the top of the flat top, insuring that the interface between the film and the silicon wafer was in the center of the flat top. The wedge was then adhered to it by using Pt deposition. Once the wedge was secured to the post, the ion beam was used to slice this welded part off from the rest of the specimen. This was repeated five more times until six samples had been created from one wedge. The microtip coupon was then compucentrically rotated 180° so Pt could be deposited onto the other side of the mounted samples, completing the adhesion process. These mounted samples were then milled into appropriate atom probe specimens by applying a sequence of annular milling patterns, ensuring that the interface region of interest was in the center of the tip, in order to thin the sample into a long needle-like specimen with a tip radius of about 100 nm. A low-keV cleaning mill was used to remove any Ga implantation that may have occurred.

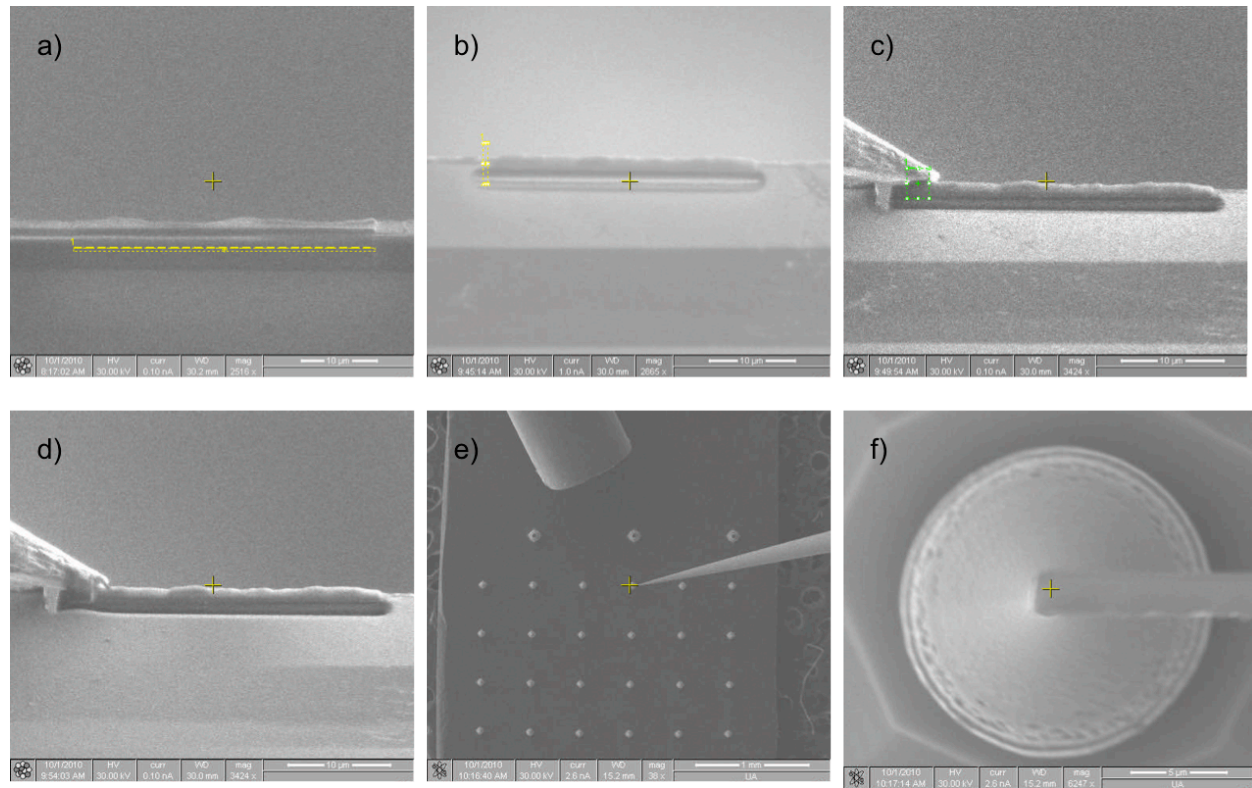


Figure 2.8 APT In-Situ Tip Preparation, Parallel Orientation

2.2.5 Atom probe tomography

The atom probe tips were field evaporated in a Cameca Local Electrode Atom Probe (LEAP) 3000XSi. The field evaporation experiment was carried out under various conditions to determine the optimal field evaporation behavior, indicated by a reduction of fracture failures, the total number of collected ions, and if reconstruction aberrations were more or less apparent. The optimal voltage pulsing conditions for the Fe-Ni were at 40 K, 200 kHz, 20% pulse fraction, and a 0.5% evaporation rate. The optimal voltage pulsing conditions for the Ti-Nb were at 60 K, 200 kHz, 20% pulse fraction, and a 0.5% evaporation rate. These conditions were optimized by systematically changing the temperature from 30 K up to 60 K and by systematically changing the evaporation rate from 0.2% up to 0.8%. The experiments that consistently yielded the highest number of collected atoms were identified as the most ideal conditions for these materials. The collected data was then analyzed using the IVAS 3.4.1 software package.

2.3 TEM Correlation of APT Evaporation

Since the reconstruction algorithms in place assume a constant radius of curvature across the apex of the field evaporation specimen, the reconstructed data for the specimen geometry featuring the layer interfaces oriented parallel to the evaporation direction can only begin to be free of artifacts if this assumption is valid. In order to determine the validity of this, a Fe/Ni tip and a Ti/Nb tip were evaporated under the conditions determined above. After several million ions were evaporated and collected, the experiment was stopped in order to observe the tip shape. In order to do this, the microtip coupon was placed in the FIB, and the ex-situ

manipulator was adhered to the base of the tip using the GIS Pt source. A cut was then made through the full thickness of the base just below the deposited Pt. This tip was then lifted from the microtip coupon and attached to the top of a Cu Omniprobe grid using the GIS Pt source within the FIB. Since this tip was sharpened for atom probe characterization, no thinning was needed since it should already be electron transparent. This process is shown in a step-by-step manner in Figure 2.9, below. These Cu Omniprobe grids were then characterized in a FEI Tecnai F20 Transmission Electron Microscope with a 200 keV Field emission electron source in order to observe the continuity of the curvature at the layer interfaces.

2.4 Experimental evaporation simulations

2.4.1 TipSim

In order to understand what types of evaporation behaviors can be expected from different combinations of elements within a specimen tip, simulations were performed. Cameca's TipSim was the simulation software utilized for this experiment. Models of tip field evaporation, propagation subject to local magnification effects, and basic detection efficiencies were incorporated into this piece of software [38].

The primary evaporation simulation is an evolving electrostatic potential simulation based on a finite relaxation solution of Poisson's equation [39, 40]. The primary geometry defining the domain of the simulation is a cubic grid consisting of wall sections, a tip section, and a vacuum section. The walls and the tip are treated as boundary conditions in the sense that they are given fixed potentials. The vacuum section contains potentials, which are calculated based on the boundary conditions specified at the walls and the tip. In the simulation, evaporation consists of selecting one or more atoms to remove. If the atoms are part of the analysis, they

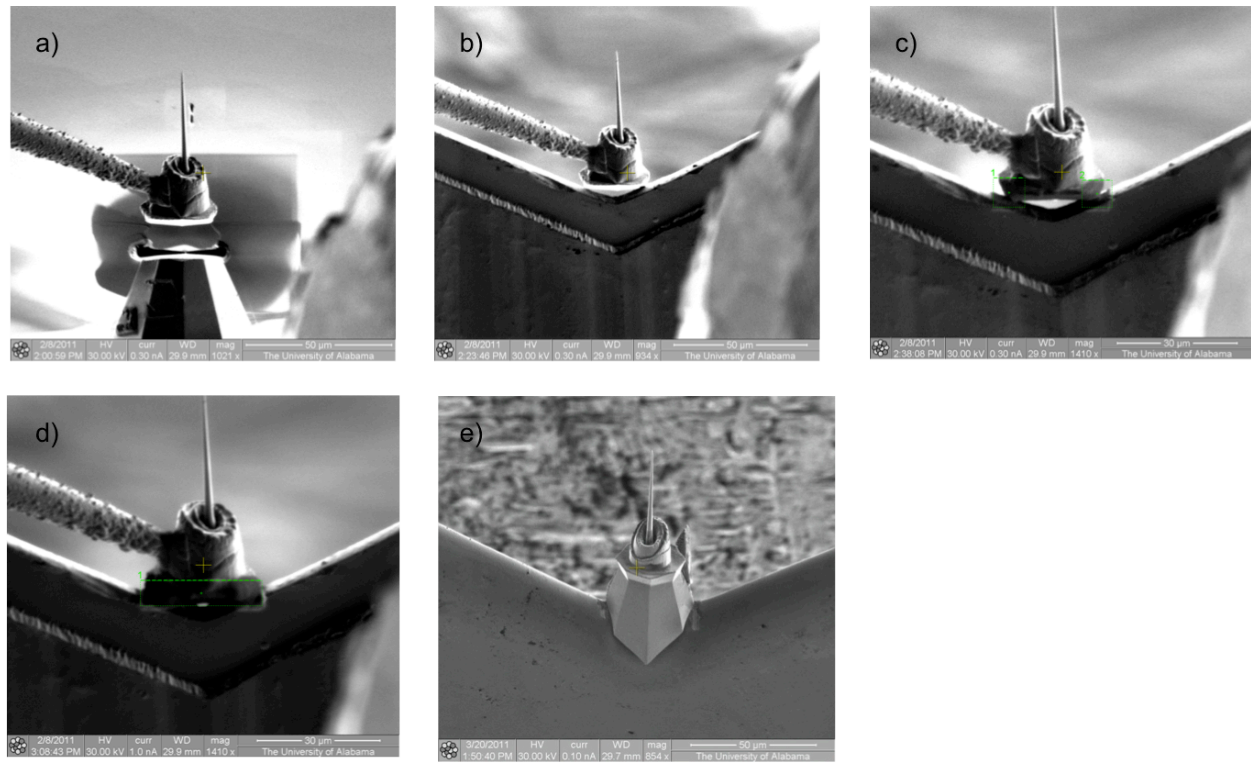


Figure 2.9 APT Tip Extraction for TEM Tip Shape Analysis

will be propagated through the calculated potential volume, and when they reach the edge of the simulation volume, they are projected to a detection plane. Mechanisms within the code are provided for specifying volume and tip geometry, material properties, pulser properties and control, detector geometry, and detector efficiency [38].

For this specific work, TipSim was used in order to observe the evaporation behavior within Fe/Ni multilayers with a 4 nm bilayer spacing mounted in the perpendicular and parallel limiting geometries. The number of layers, layer thickness, layer field strength, and layer mass were inputted by the user into this software. The tip height, shank angle, number of ions to evaporate, and the pulse fraction were also user entered to allow for the simulation to be as close to the parameters used in real experimentation as possible.

2.4.2 SRIM

In order to understand how FIB preparation of these tips can become an issue based on the gallium implantation and milling procedures, Stopping and Range of Ions in Matter (SRIM) simulations were performed. SRIM is a group of simulation software programs that calculate the stopping power and range of ions into matter using a kinetic Monte Carlo approach to treat each of the ion-to-atom collisions. This calculation utilizes statistical algorithms which allow the ion to make jumps between calculated collisions and then averaging the collision results over the imposed gap, allowing the software to be efficient. During these collisions, the ion and the atom have a screened Coulomb collision, including exchange and correlation of interactions between the overlapping electron shells. The ion has long range interactions, creating electron excitations and plasmons within the target. To describe this, a description of the target's collective electronic structure and inter atomic bond structure is included during set-up. The

charge state of the ion within the target is described using the concept of effective charge, which includes a velocity dependent charge state and long range screening due to the collective electron sea of the target [41].

This software allows the user to generate a specimen—in this case Fe and Ni layers simulated in a 4 nm bilayer spacing in both the parallel and perpendicular limiting geometries were exposed to a flux of gallium ions to determine the degree of intermixing that can be imposed on the sample during the preparation process. The user can then identify how many gallium atoms are to strike a specific point on the surface. Upon completion, the software outputs the movement of the implanted atoms, the displacement of atoms within the sample, and a two-dimensional map of the sample before and after exposure.

CHAPTER 3

RESULTS

3.1 TEM phase identification

The equilibrium structures of Fe, Ni, Ti, and Nb at one atmosphere and room temperature are body-centered cubic, face-centered cubic, hexagonal close packed, and body-centered cubic, respectively [42]. Even though Fe and Ni typically exhibit different crystal structures, when the Fe/Ni multilayered thin film was conventionally prepared, into a plan-view TEM foil for diffraction analysis, the selected area diffraction pattern showed a single phase, as shown in Figure 3.1(a). This single phase was identified as FCC, identified by all of the reflected planes being all unmixed—all even or all odd h , k , l values [33]. This was determined by taking the ratio of the first two measured reflection rings and comparing this to the ratio allowed for diffraction of FCC and BCC. In this particular case, since the Ratio was 598:521 pixels, this meant that the Fe adopted the crystal structure of the Ni layers and had allowed reflections from the {111} and {200} planes. This was determined by utilizing Bragg's Law for electron diffraction. Bragg's law allowed the user to be able to determine the d-spacing of the diffracted rings by measuring their respective distances from the transmitted beam within the diffraction patterns as shown in Figure 3.1(a). While the diffraction pattern shows only one phase, there are obviously two distinct layers within the film, as shown in the HAADF-STEM image in Figure 3.2(a).

After determining the typically body-centered cubic Fe adopted the face-centered cubic structure of Ni, the same analysis was performed on the Ti/Nb multilayers in order to determine if there was a phase change as well. A plan-view TEM foil was fabricated using traditional

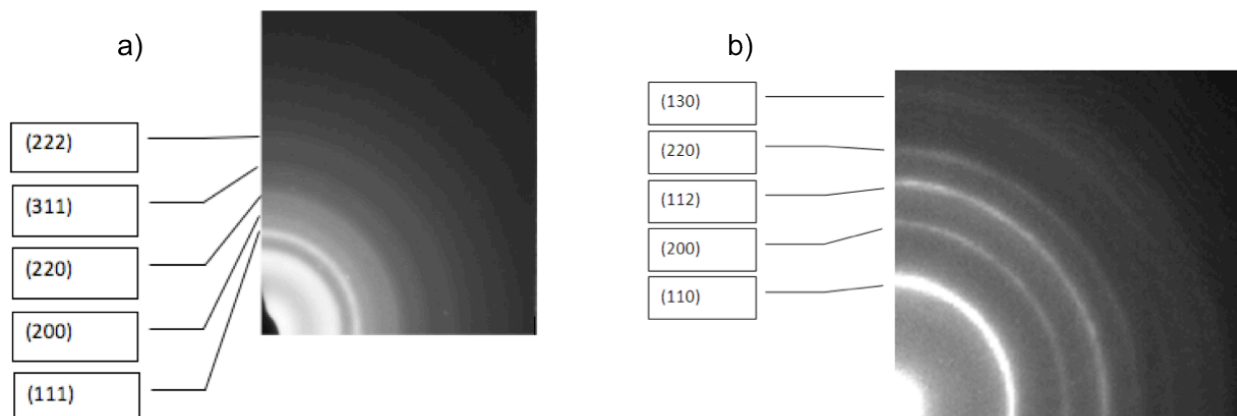


Figure 3.1 Multi-Crystalline TEM Diffraction Patterns

- a) Fe/Ni Multilayered Thin Film
- b) Ti/Nb Multilayered Thin Film

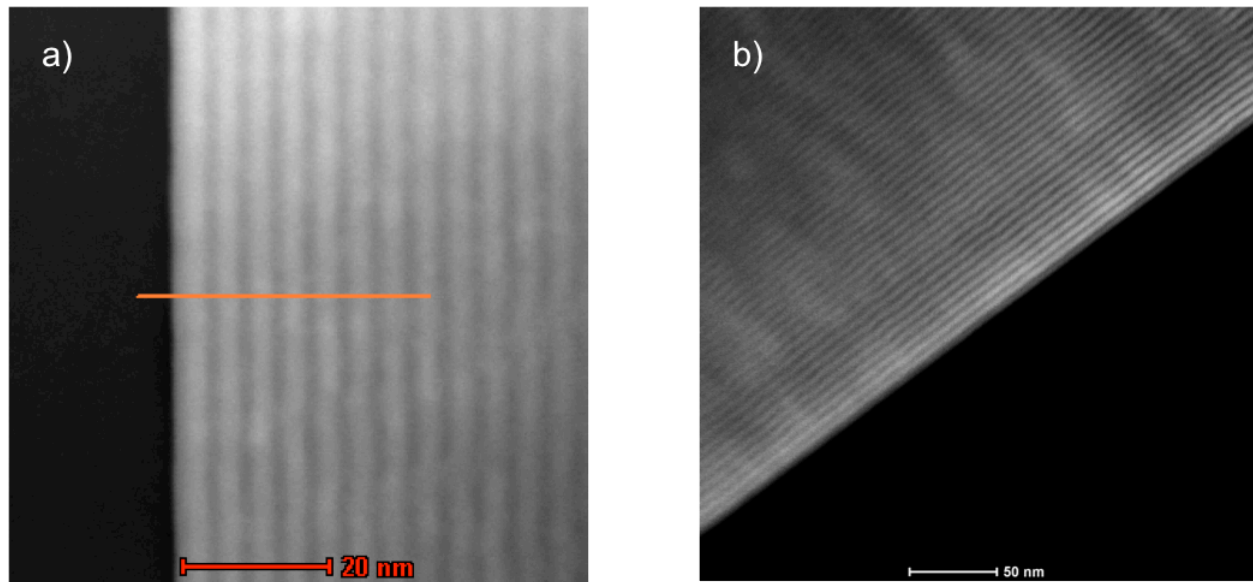


Figure 3.2 HAADF-STEM Images

- a) Fe/Ni Multilayered Thin Film
- b) Ti/Nb Multilayered Thin Film

techniques, and it was characterized in the TEM using selected area diffraction patterns. As shown in Figure 3.1(b), the multilayered film adopted a body-centered cubic structure, shown by all of the reflected planes having an even sum of the h,k,l values [32]. While the multilayers exhibited a diffraction pattern of one phase, there are obviously 2 separate layers, as shown in Figure 3.2(b). In this particular case, the ratio of the first two measured reflection rings correlated to allowed reflections from the {110} and {200} planes. This was also determined by utilizing Bragg's Law for electron diffraction. Bragg's law allowed the user to be able to determine the d-spacing of the diffracted rings by measuring their respective distances from the transmitted beam within the diffraction patterns as shown in Figure 3.1(b). Simply put, this means that the Ti adopted the equilibrium crystal structure of its Nb counterpart. This, however, is not a surprise since it was also seen in the research performed by Genc [7].

3.2 Electron energy loss spectroscopy

A representative cross-section HAADF STEM image of the Fe/Ni multilayer thin film is shown in Figure 3.2(a). In this image, the layers with the greater atomic number, Ni ($Z_{\text{Ni}} = 28$), appear brighter, and the Fe ($Z_{\text{Fe}} = 26$) layers are darker because of their lower atomic number. The EELS compositional profile for this set of layer pairs was taken from the center of this image, in the direction normal to the layer interfaces. This computed profile, shown in Figure 3.3, is the result of the background subtraction and the relative composition calculations. From this profile, the thicknesses for both the Fe and the Ni elemental layers could be determined. As shown in Table 3.1, the average thickness of the Fe layers in the sample was 2.07 nm, and the average thickness of the Ni layers in the sample was measured to be 2.12 nm. These values and

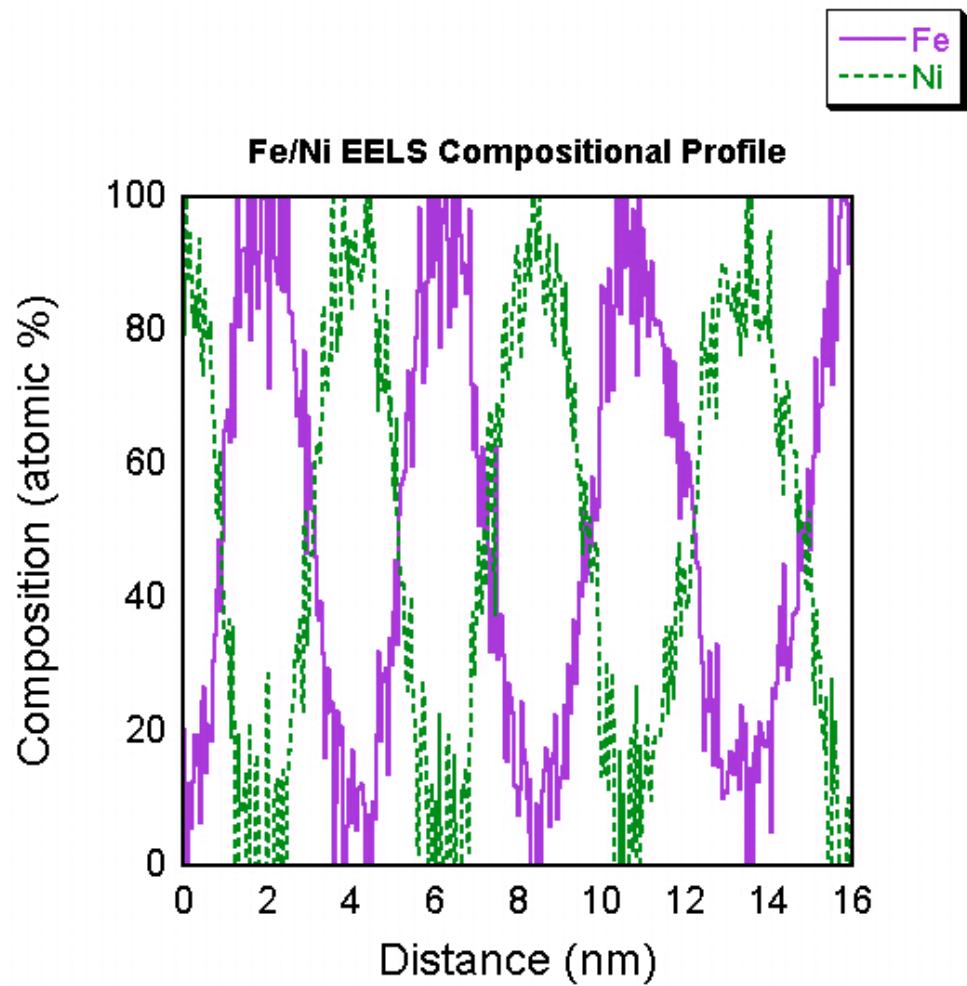


Figure 3.3 Fe/Ni EELS Compositional Profile

Table 3.1 Measured Elemental Layer Thicknesses from Across Different Characterization Techniques

Measured Layer Thickness (nm)			
	EELS	APT Parallel	APT Perpendicular
Fe	2.07 ± 0.25	3.75 ± 0.24	1.89 ± 0.07
Ni	2.12 ± 0.11	1.89 ± 0.01	2.19 ± 0.17
Ti	1.65 ± 0.10	1.69 ± 0.16	0.67 ± 0.11
Nb	3.60 ± 0.16	5.09 ± 0.19	1.97 ± 0.01

atomic positions are considered to be the ‘true’ compositional modulation for this multilayer system from which the reconstructed atom probe data would be compared.

A representative cross-section HAADF STEM image of the Ti/Nb multilayered thin film is shown in Figure 3.2(b). Within this image, the layers with the greater atomic number, Nb ($Z_{Nb} = 41$), appear brighter, and the Ti ($Z_{Ti} = 22$) layers are darker) [33]. Unlike in the Fe/Ni films, a specific composition was unable to be identified within the film. Instead, the areal density was quantified as a function of atoms per area. This is because there is not a recorded ionization cross-section for niobium that can be used as a standard. For this analysis, as described in Chapter 2, since niobium is a relatively high-Z element, the M edge had to be used instead of the L edge. This edge exhibits a slow onset in contrast to the sharp peak the L edges exhibit. Also, since it has such a high atomic number, this M edge cannot be modeled like it can be for the K or L edge in other materials. If a standard were present, then a compression factor could be generated much like in EDS analysis to determine the actual edges, and the actual composition could be acquired.

Much like in the Fe/Ni system, the EELS compositional profile for this set of layer pairs was taken from the center of this image, in the direction normal to the layer interfaces. The computed profile, shown in Figure 3.4, is the result of the background subtraction and the relative composition calculations. From this profile, the thicknesses for both the Ti and Nb elemental layers could be determined to be 1.65 nm and 3.60 nm, respectively. This data has been tabulated in Table 3.1. As above, these values and atomic positions are considered to be the correct data for this multilayer.

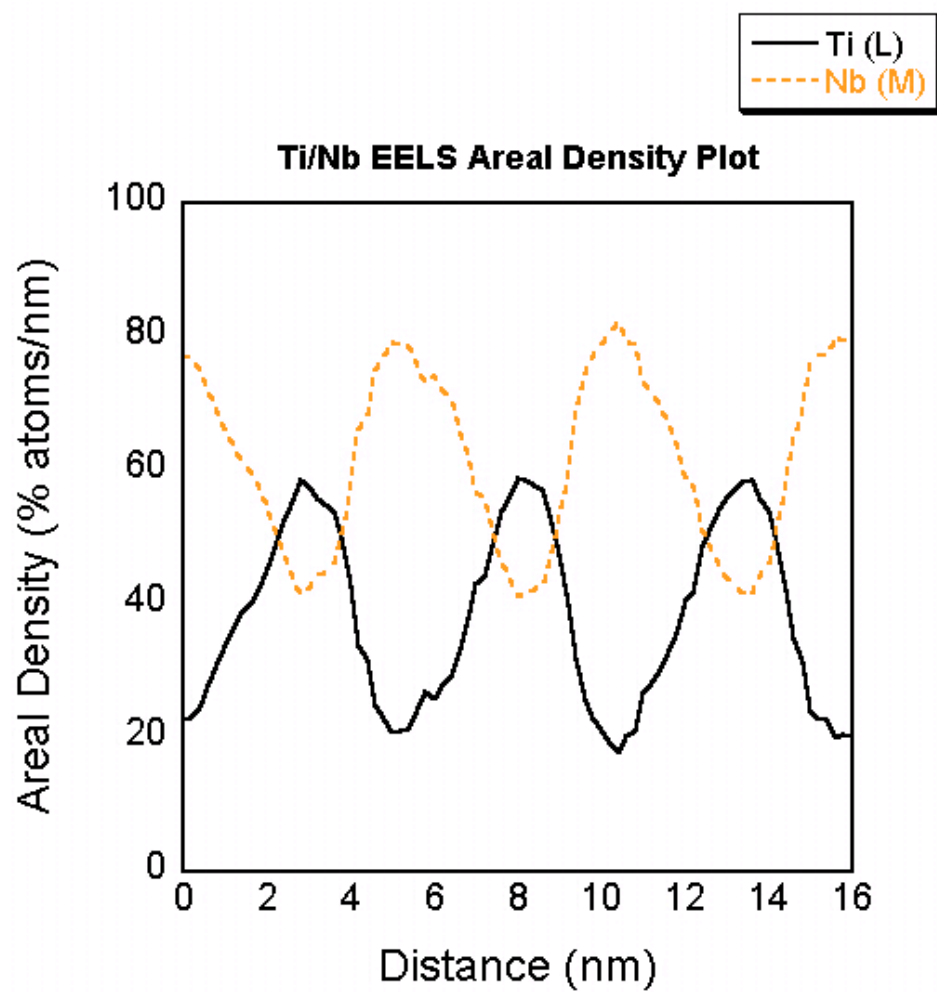


Figure 3.4 Ti/Nb EELS Areal Density Core-Loss Profile (atoms/nm²)

3.3 APT in the perpendicular orientation

After collecting the data using the procedure outlined in previous sections, the next step was to reconstruct the data into representative atom maps by utilizing the IVAS 3.4.1 software. The first step in this reconstruction process was to select the range of ions from which to build the reconstruction using the voltage history as shown in Figure 3.5. Next, the region of the detector from which atoms were collected is identified, and a corrected time of flight (TOF) spectrum is obtained, as shown in Figure 3.6. Next, the mass spectrum is adjusted to fit the known elements within the sample, and the peaks are identified and linked to a specific element, as shown in Figure 3.7. Finally, the k-factor, image compression factor, initial radius, and estimated shank half angle are identified in order to create a digital reconstruction of the tip.

The reconstructed atom maps for the Fe/Ni and Ti/Nb tips with the chemical modulations field evaporated in the perpendicular or layer-by-layer geometry are shown in Figure 3.8(a) and Figure 3.8(b), respectively. For both of these data sets, the flight path was identified as 90 mm due to the construction of the LEAP. For these samples, the k-factor was identified as 3.30, and the image compression factor used was 1.65. The identified initial radius was 30.22 nm, and the computed shank half angle was 11.3°. For the Ti/Nb sample, the initial radius was identified as 38.79 nm and the estimated shank half angle was 14.4°. The 50 atomic % Fe iso-concentration surfaces were created in order to generate surface proximity histograms or proxigram; a representative proxigram is shown in Figure 3.9 [43]. From this compositional profile, the thicknesses of the individual elemental layers were measured to be 1.89 and 2.19 nm for Fe and Ni layers, respectively, and are tabulated into Table 3.1. The 50 atomic % Ti iso-concentration surfaces were created to calculate surface proxigrams; a representative proxigram is shown in Figure 3.10 [43]. From this compositional profile, the thicknesses of the individual elemental

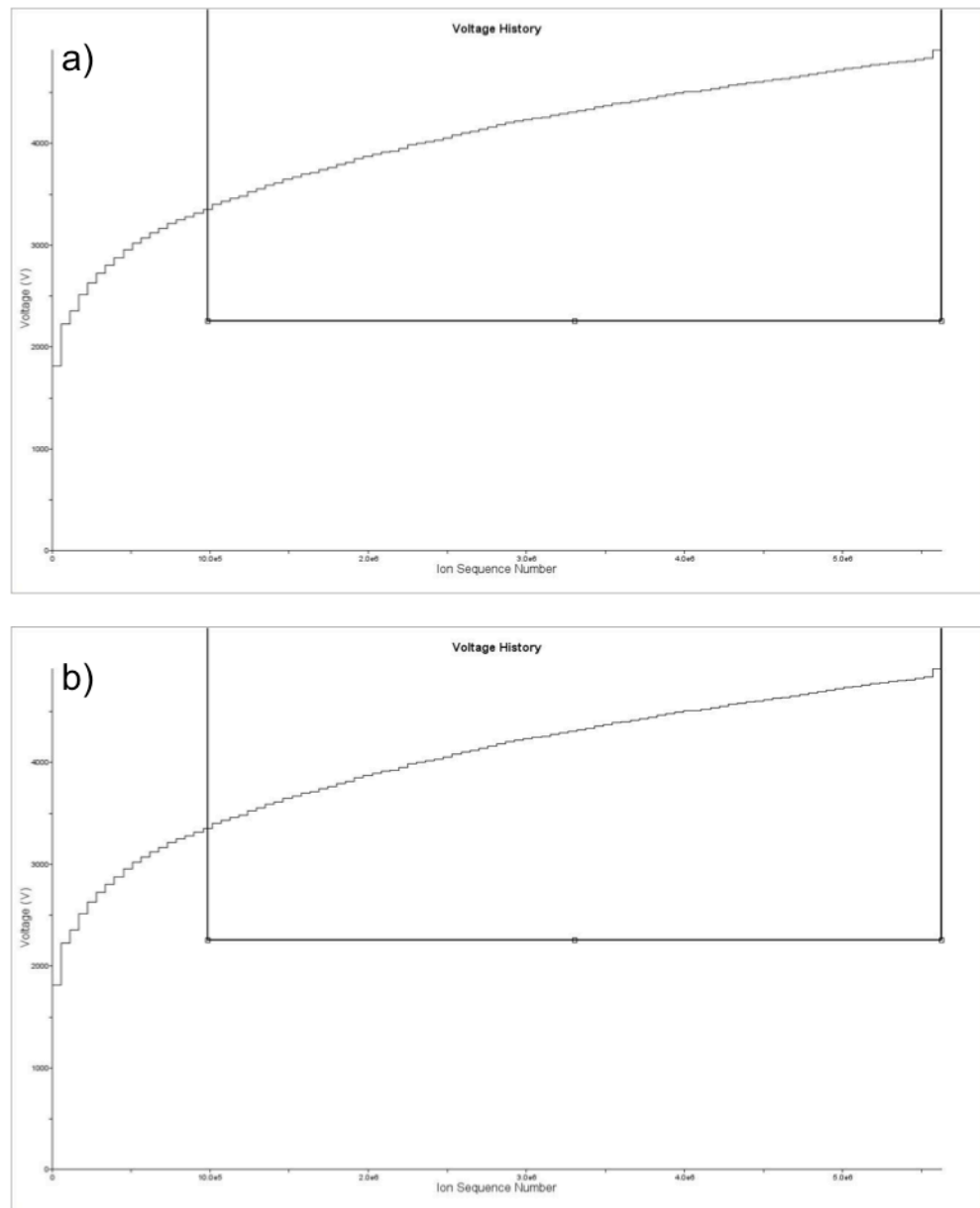


Figure 3.5 APT Voltage Histories from the Perpendicular Orientations

- a) Fe/Ni Multilayered Thin Film
- b) Ti/Nb Multilayered Thin Film

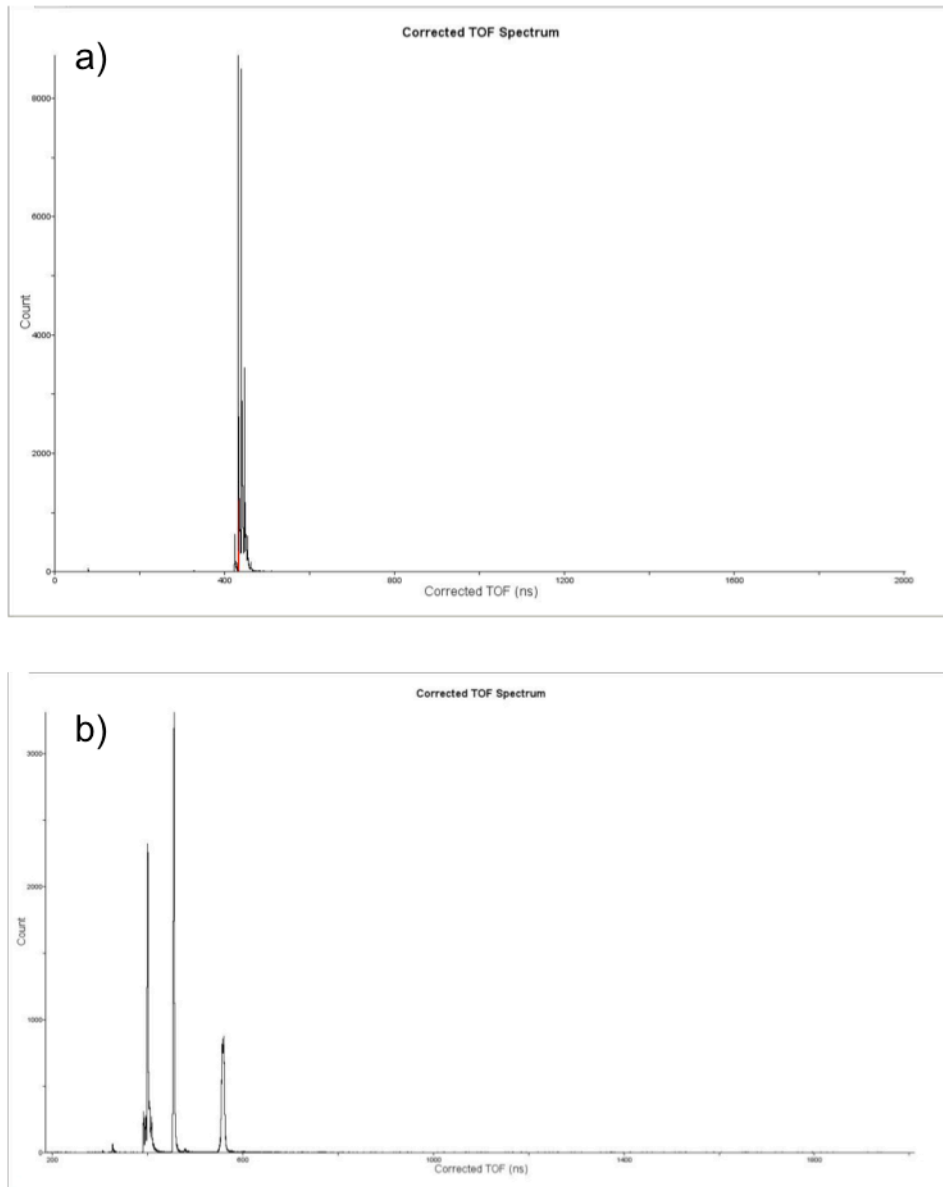


Figure 3.6 APT Corrected Time-of-Flight Spectrums from Perpendicular Orientations

- a) Fe/Ni Multilayered Thin Film
- b) Ti/Nb Multilayered Thin Film

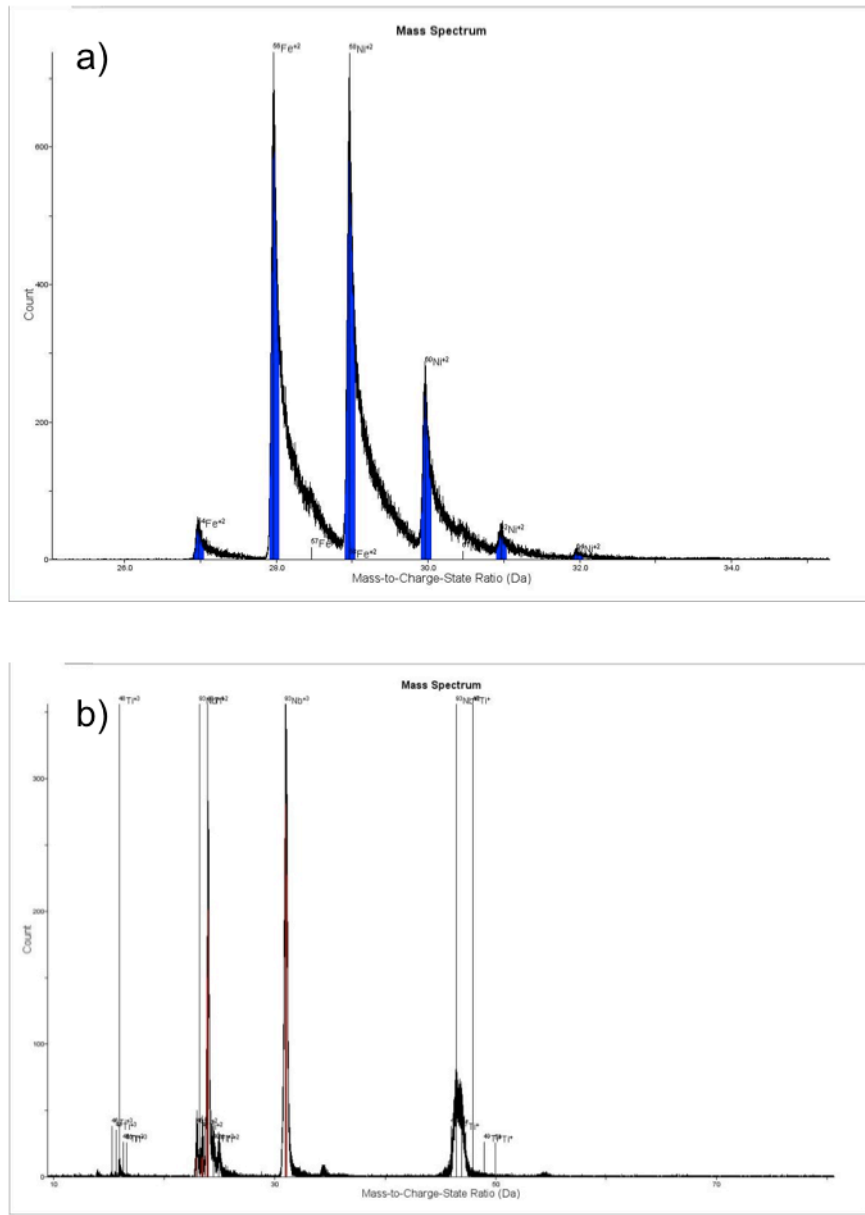
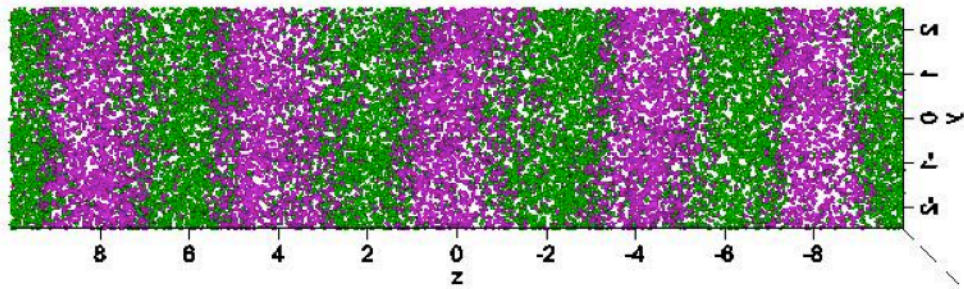


Figure 3.7 APT Mass Spectrums from the Perpendicular Orientations

a) Fe/Ni Multilayered Thin Film

b) Ti/Nb Multilayered Thin Film

a)



b)

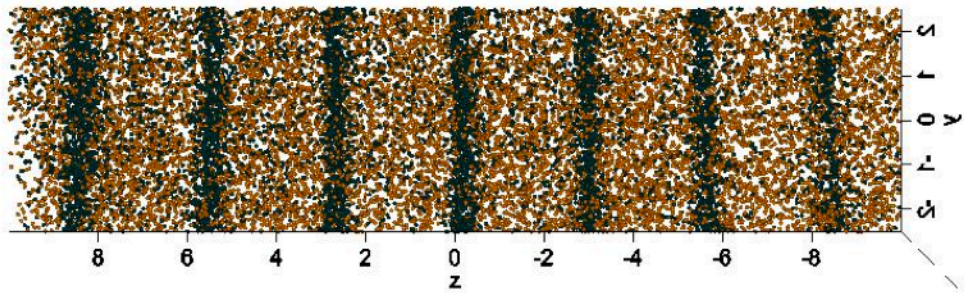


Figure 3.8 APT Reconstructed Atom Maps from the Perpendicular Orientation

- a) Fe/Ni Multilayered Thin Film
- b) Ti/Nb Multilayered Thin Film

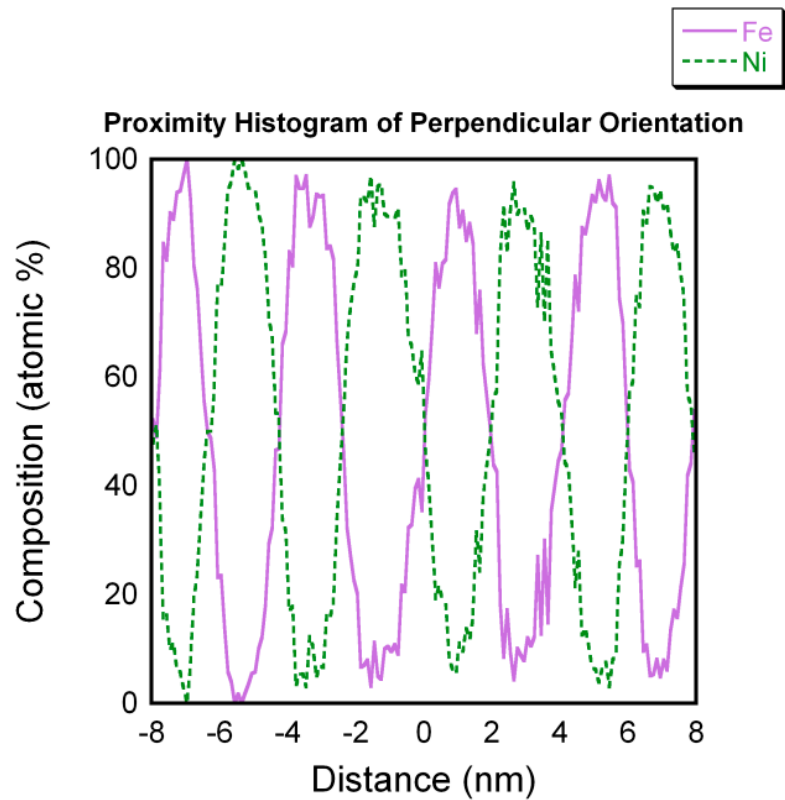


Figure 3.9 Fe/Ni Perpendicular APT Proximity Histogram
(Distance of 0 Defines Surface from which Proxigram was Measured)

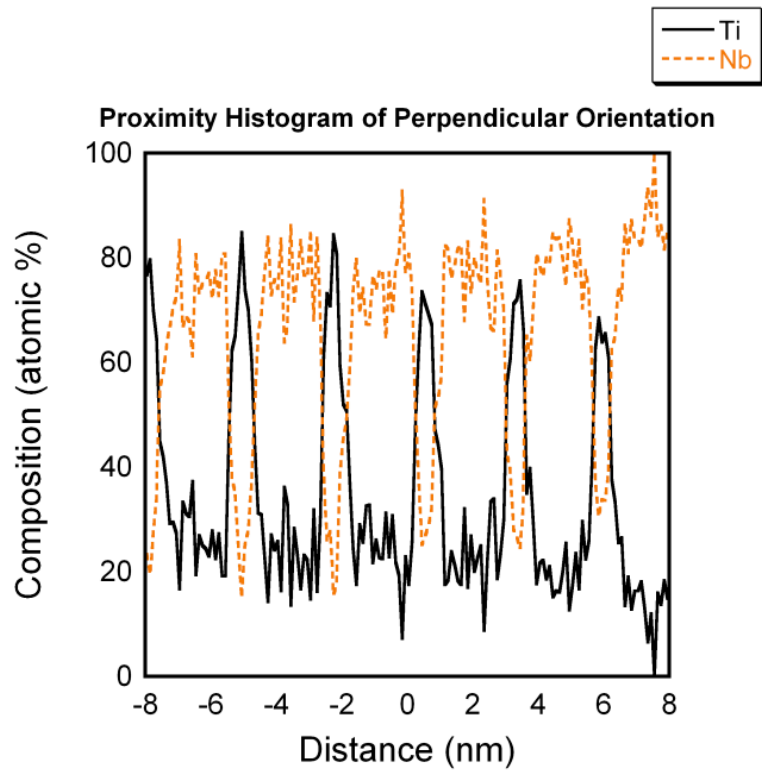


Figure 3.10 Ti/Nb Perpendicular APT Proximity Histogram
(Distance of 0 Defines Surface from which Proxigram was Measured)

layers were measured to be 0.67 nm and 1.97 nm for the Ti and Nb, respectively, and are tabulated into Table 3.1.

3.4 APT in the parallel orientation

Much like above, after collecting the data using the procedure outlined in previous sections, the next step was to reconstruct the data into representative atom maps by utilizing the IVAS 3.4.1 software. The first step in this reconstruction process was to select the range of ions from which to build the reconstruction using the voltage history as shown in Figure 3.11. Next, the region of the detector from which atoms were collected is identified, and a corrected time of flight (TOF) spectrum is obtained, as shown in Figure 3.12. Next, the mass spectrum is adjusted to fit the known elements within the sample, and the peaks are identified and linked to a specific element, as shown in Figure 3.13. Finally, the k-factor, image compression factor, initial radius, and estimated shank half angle are identified in order to create a digital reconstruction of the tip.

The reconstructed atom maps for the Fe/Ni and Ti/Nb tips with the chemical modulations field evaporated in the perpendicular or layer-by-layer geometry are shown in Figure 3.14(a) and Figure 3.14(b), respectively. For these samples, the k-factor was identified as 3.30, and the image compression factor was 1.65. For the Fe/Ni sample, the initial radius used was 45.0 nm, and the estimated shank half angle was 18.7°; the initial radius for the Ti/Nb sample was 33.05 nm, and the estimated shank half angle was 10.5°. The 50 atomic % Fe iso-concentration surfaces were created in order to generate proxigrams from the experimental evaporation data; a representative proxigram is shown in Figure 3.15 [43]. From this compositional profile, the thicknesses of the individual elemental layers were measured to be 3.75 and 1.89 nm for Fe and Ni layers, respectively, and are tabulated into Table 3.1. The 50 atomic % Ti iso-concentration

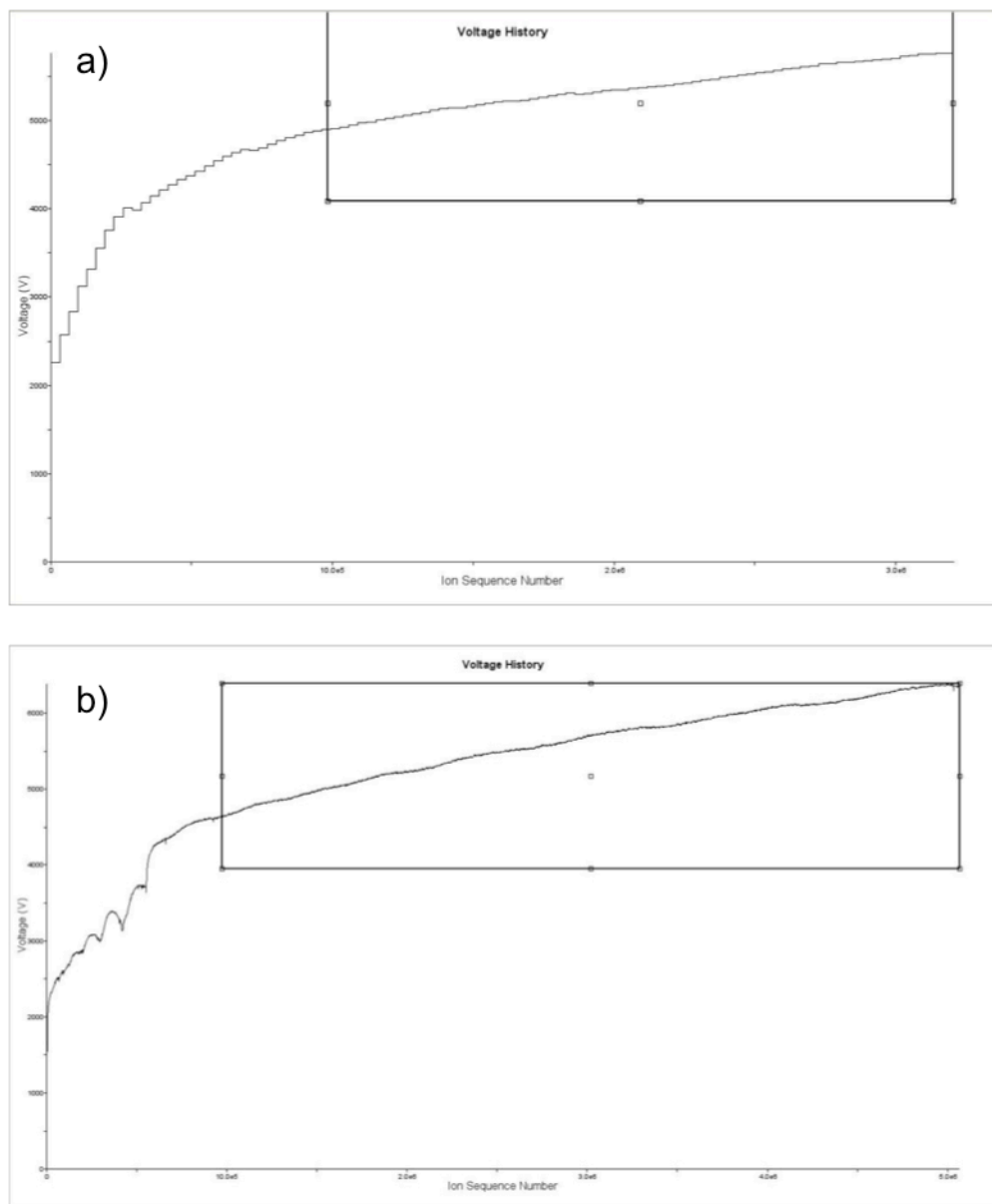


Figure 3.11 APT Voltage Histories from the Parallel Orientations
 a) Fe/Ni Multilayered Thin Film
 b) Ti/Nb Multilayered Thin Film

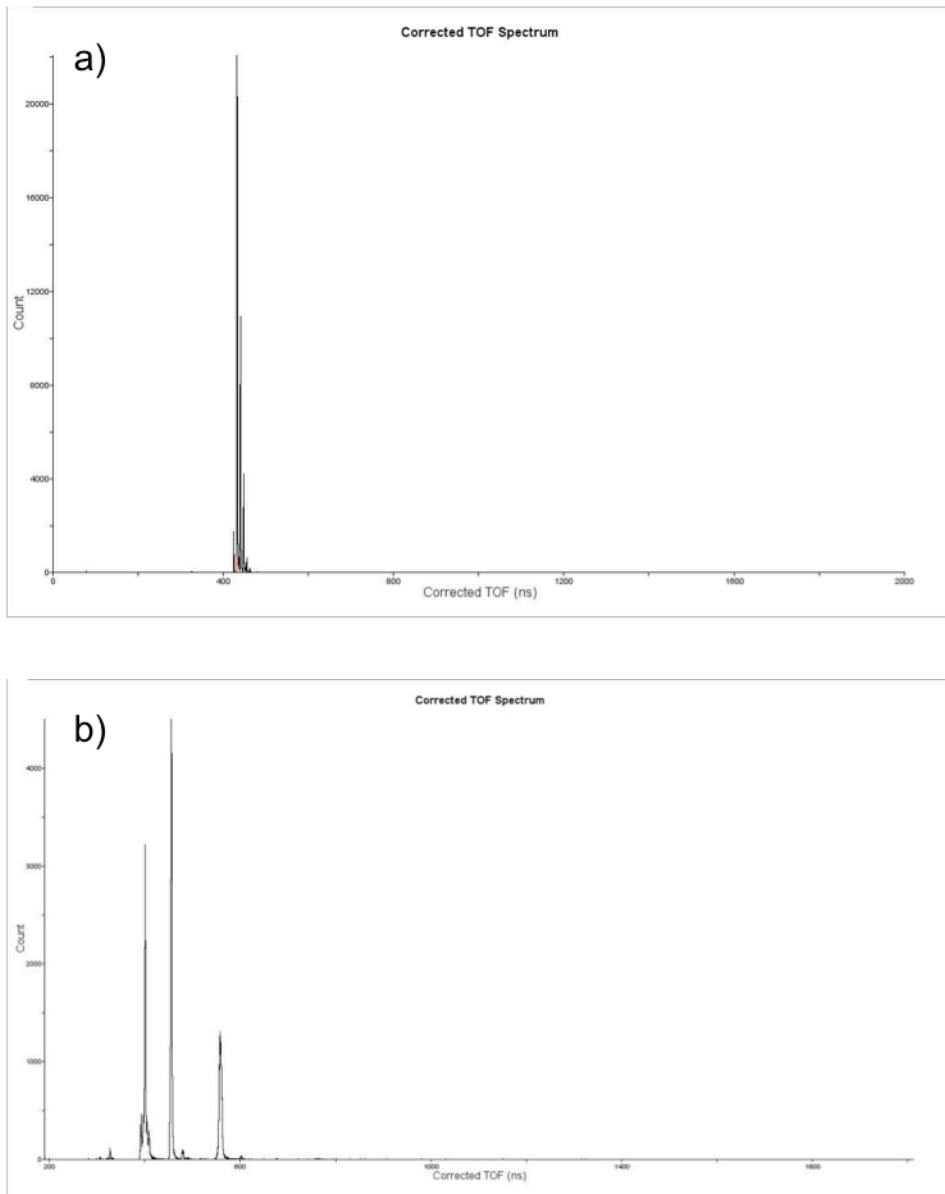


Figure 3.12 APT Corrected Time-of-Flight Spectrums for the Parallel Orientations

- a) Fe/Ni Multilayered Thin Film
- b) Ti/Nb Multilayered Thin Film

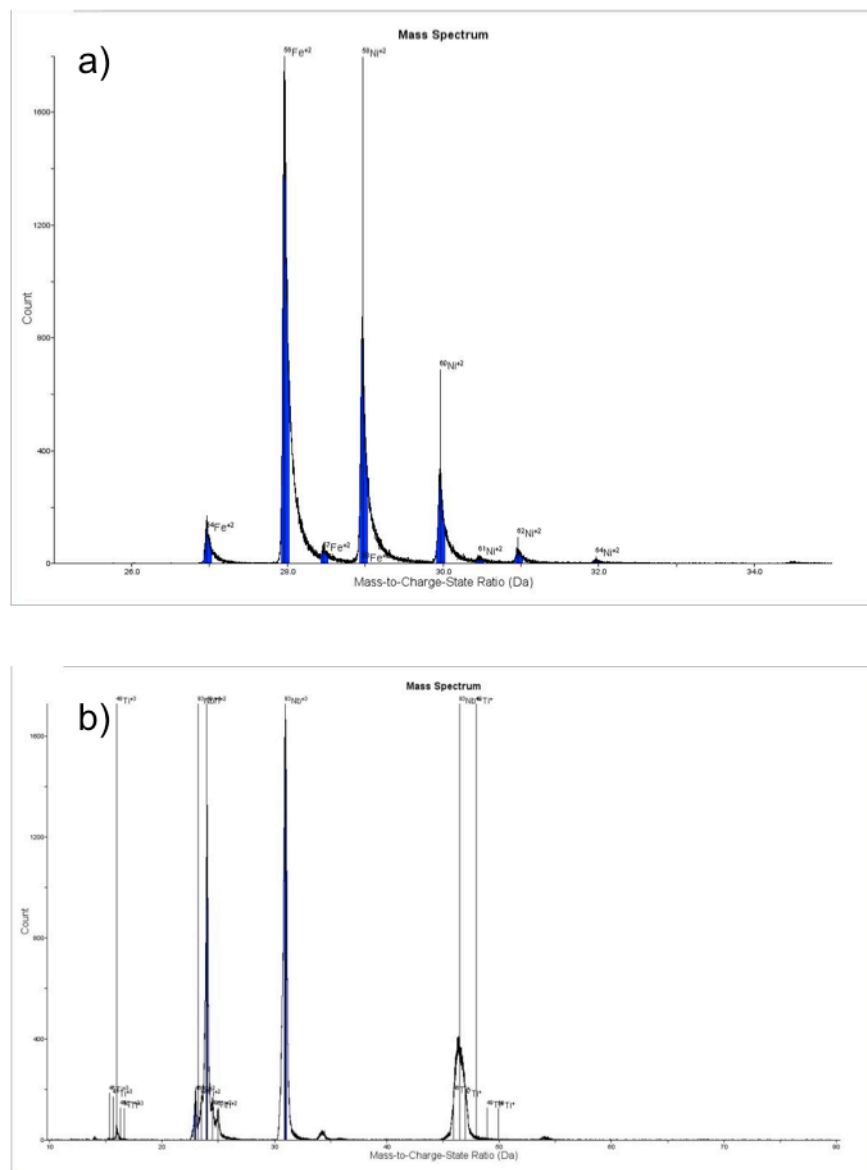


Figure 3.13 APT Mass Spectrums from the Parallel Orientations

a) Fe/Ni Multilayered Thin Film

b) Ti/Nb Multilayered Thin Film

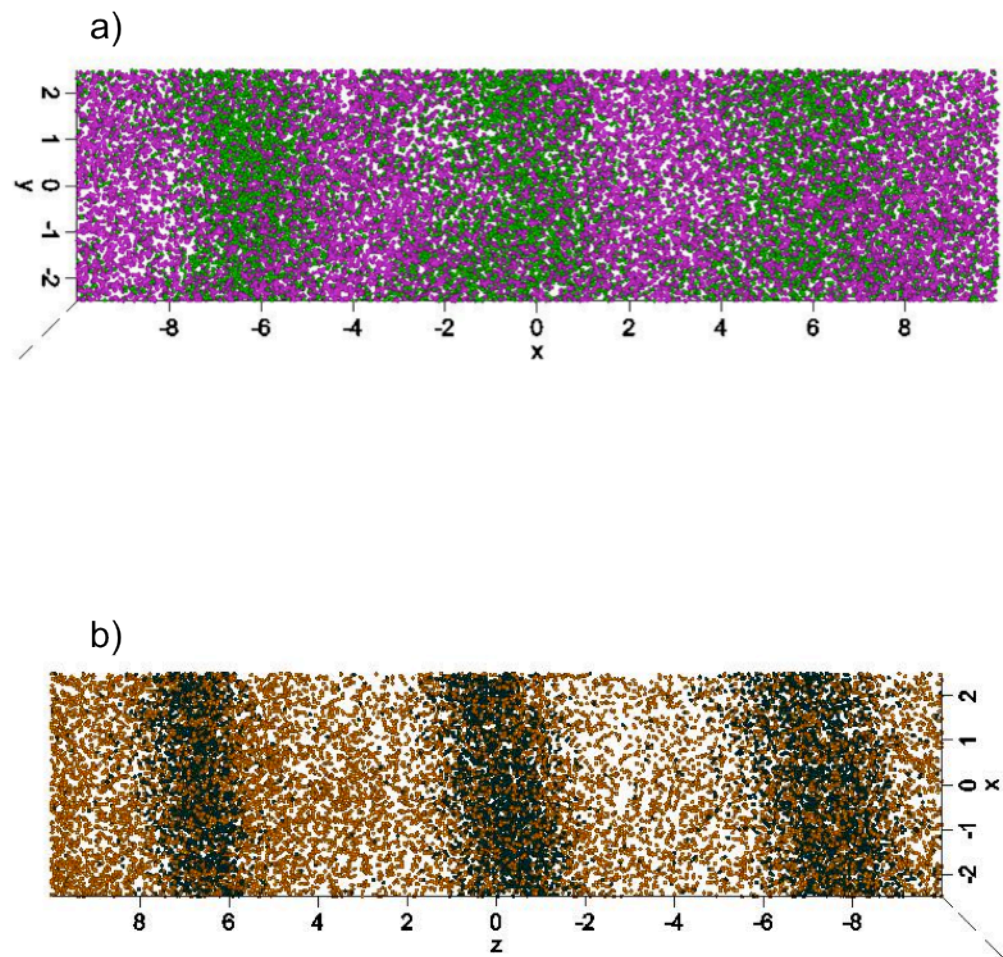


Figure 3.14 APT Reconstructed Atom Maps in the Parallel Orientations

- a) Fe/Ni Multilayered Thin Film
- b) Ti/Nb Multilayered Thin Film

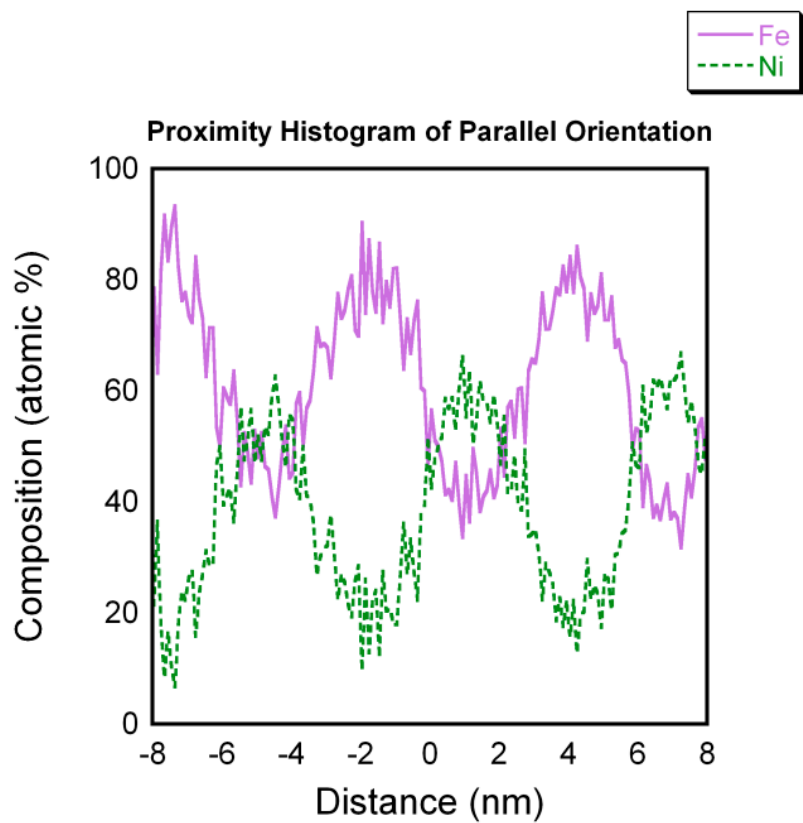


Figure 3.15 Fe/Ni Parallel APT Proximity Histogram
(Distance of 0 Defines Surface from which Proxigram was Measured)

surfaces were created to calculate surface proxigrams; a representative proxigram is shown in Figure 3.16 [43]. From this compositional profile, the thicknesses of the individual elemental layers were measured to be 1.69 nm and 5.09 nm for the Ti and Nb, respectively, and are tabulated into Table 3.1.

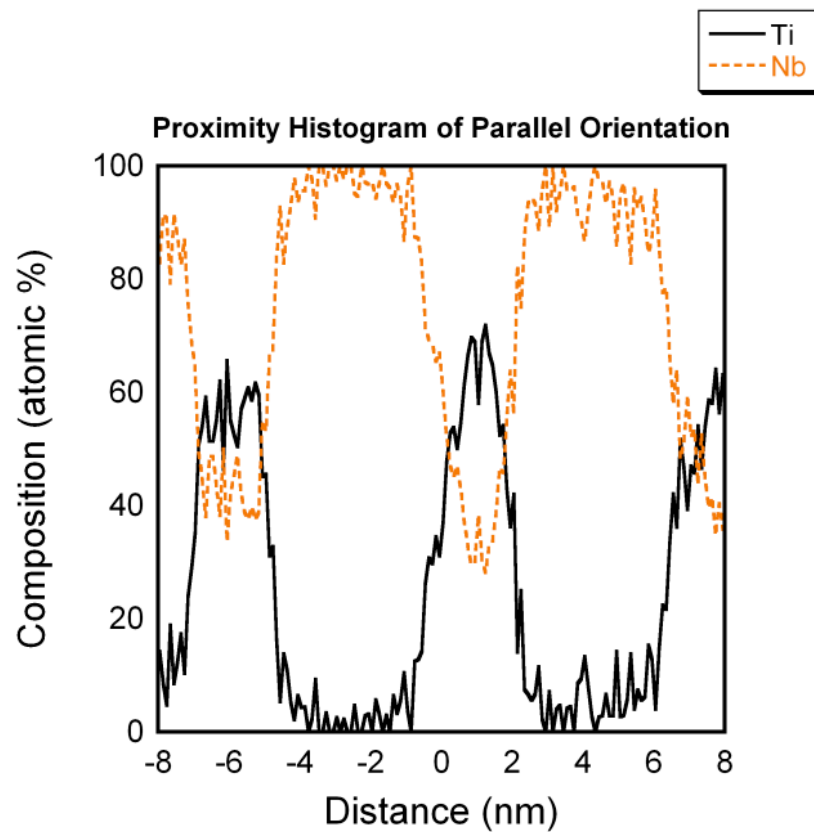


Figure 3.16 Ti/Nb Parallel APT Proximity Histogram
(Distance of 0 Defines Surface from which Proxigram was Measured)

CHAPTER 4

DISCUSSION

4.1 Phase change behavior

Plan-view electron diffraction patterns provided a useful orientation phase identification due to the ability for the TEM to image through the several layers of the material. The d-spacing values associated with each of the {hkl} diffraction rings were calculated by measuring each of the projected radii and applying them individually into Equation 2.1. Typically, at ambient temperatures and pressures, Fe has a body-centered cubic crystal structure with a lattice parameter of 2.87 angstroms, Ni has a face-centered cubic crystal structure with a lattice parameter of 3.52 angstroms, Ti has a hexagonal close-packed crystal structure with lattice parameters of 2.95 and 4.68 angstroms, and Nb has a body centered cubic crystal structure with a lattice parameter of 3.30 angstroms.

The diffraction patterns from these multilayered thin films, however, show only one crystal structure for each multilayer film. In the case of the Fe/Ni film, this arrangement was found in Ni's typical face-centered cubic structure. When the two elements were sputtered on top of one another, the Fe atoms, which can exhibit face-centered cubic structure at elevated temperatures and pressures, experienced a phase change in order to intermix with the Ni atoms. In the case of the Ti/Nb film, the packing arrangement was found to be in Nb's typical body-centered cubic structure. The Ti atoms, when sputtered sequentially with Nb, experienced a phase transformation into its high temperature form of body-centered cubic. This allowed the Nb to intermix into the Ti elemental layers.

The phase changes exhibited in the Fe/Ni and Ti/Nb systems, in particular, were possible due to intermixing, size effects, and the lattice parameters. The intermixing, up to 20 atomic % in the Ti/Nb system functioned as a phase stabilizer to allow the Ti layers to exist in its high temperature crystal structure. The lattice parameter of body-centered cubic Nb is very similar to that of Ti, as listed above. The Fe and Ni also have very similar lattice parameters and have relatively similar atomic radii. This caused less of a deviation from the normal equilibrium energy within the respective systems [7].

4.2 Cross-correlation comparisons between EELS and APT

At these deposited layer thicknesses, approximate bilayer spacing of 4 nm, the Fe and Ti layers changed phase within their respective material system. As noted in the compositional profiles, significant intermixing occurred with the corresponding layer in each of these cases. The intermixing of Ni into Fe and Nb into Ti are found to both act as stabilizing elements for the respective changes in phase. This phase change, however, has been seen before since both Fe and Ti have the ability to be present in these crystal symmetries, although in pure form they exist at higher temperatures [7]. Because of this predilection to these specific equilibrium crystallographic states, the fact that these nanolaminates exhibit the structures is not alarming. Specifically, the phase transformation of nanolaminates containing Ti/Nb multilayers has been previously researched in detail by G.B. Thompson [44].

4.2.1 Correlation between perpendicular APT and EELS

All of the elemental modulation layer spacings measured via APT had discrepancies with its characterized counterparts, as seen in Table 3.1. In both the Fe/Ni and Ti/Nb, the

reconstructed atom maps from the perpendicular limiting geometry exhibited layered structures that more closely correlated with the collected EELS data, being used as the comparative standard for this experiment. The tip shape evolution for the parallel orientation of the Fe/Ni film does not show a strong deviation in local curvature, or humping, as shown in Figure 4.1(a). This is because of the fact that the elemental evaporation fields of the two species are much closer together, leading to a more similar energy level needed for evaporation to occur. This decreases the amount of local magnification that is seen within the reconstruction, using similar reconstruction parameters. As Schmitz discussed in detail, these local humps produce local magnifications, which produce ion trajectories that can spread or compress the data spatially under a single radius of curvature assumption [22].

This difference in reconstructed layer thickness, however, does not mean that the composition at the interface is altered due to the evaporation experiment. To perform this analysis, compositional gradients were calculated for both of these techniques across each separate layer interface. Essentially, the slope of the composition graph was calculated in atomic percent per nanometer for the Fe intermixing into the Ni layer and for the Ni intermixing into the Fe layer for the STEM-EELS profile. These two slopes were then expressed as a ratio in order to identify any differences in interfacial behavior across the techniques.

This result, depicted in Table 4.1, shows that for the STEM-EELS compositional profile for Fe/Ni, the ratio of the compositional gradients is 1.0. This result was used as a reference for comparison of later analysis of the perpendicular APT characterization technique. If the slope on each side of the interface is equal, then there is no roughening of the growth surface as a result of intermixing. The work done by Larson *et al.* investigated this issue using atom probe tomography [4]. The gradient measurement was performed in the same manner for the data

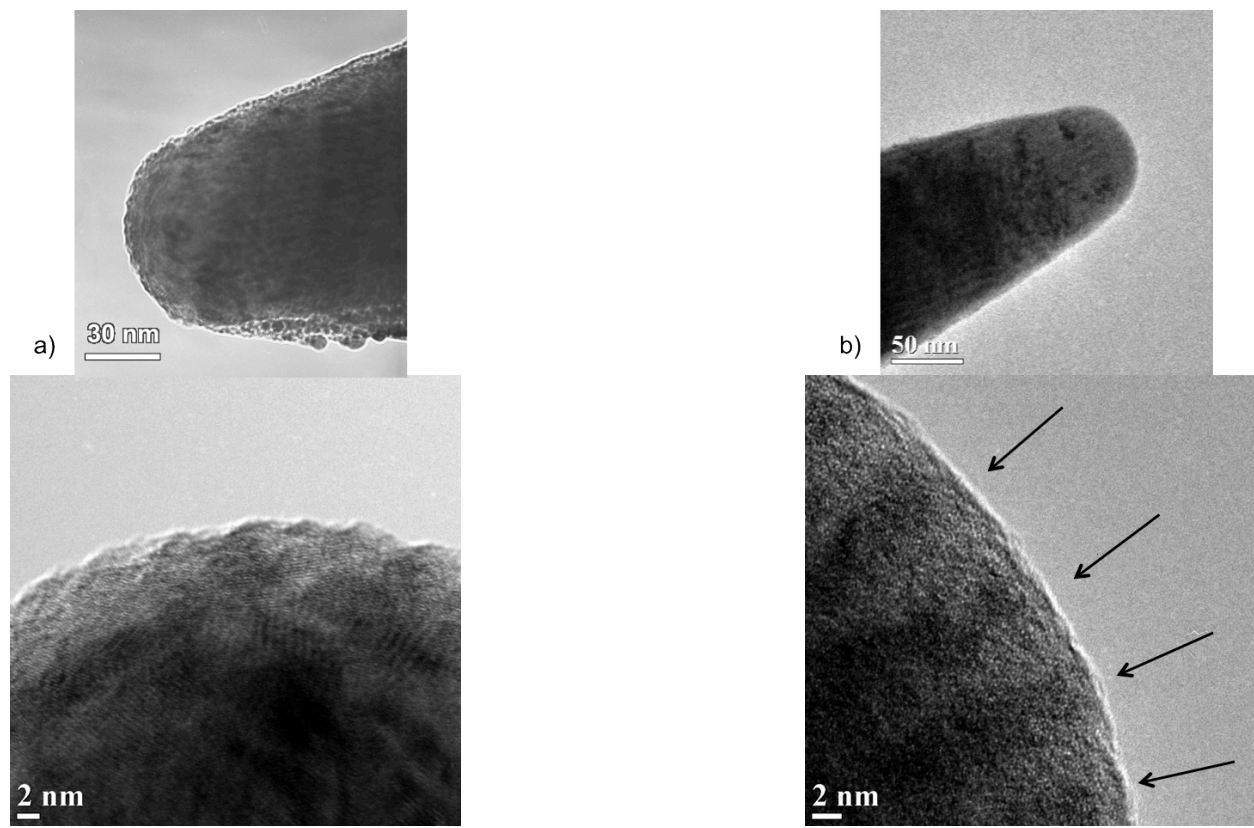


Figure 4.1 APT Tip Shape Evolutions
a) Fe/Ni Multilayered Thin Films
b) Ti/Nb Multilayered Thin Films

Table 4.1 Correlation of Compositional Gradients Across Different Characterization Techniques

Elemental Multilayers	EELS Fe on Ni (at% / nm)	EELS Ni on Fe (at% / nm)	EELS Ratio of Fe on Ni : Ni on Fe
Fe/Ni	66.3	-67.0	1.0
	EELS Ti on Nb (% atoms/nm)	EELS Nb on Ti (% atoms/nm)	EELS Ratio of Ti on Nb : Nb on Ti
Ti/Nb	21.3	-16.0	1.33
	APT Parallel Ratio Fe on Ni : Ni on Fe	APT Perpendicular Ratio Fe on Ni : Ni on Fe	
Fe/Ni	1.085	1.008	
	Ti on Nb : Nb on Ti	Ti on Nb : Nb on Ti	
Ti/Nb	1.453	0.926	

collected from the perpendicular atom probe orientation. The results of these calculations, displayed in Table 4.1, show that for the Fe/Ni films in the perpendicular geometry, the ratio of the Fe on Ni to Ni on Fe was 1.008—only a 0.8% deviation from the reference EELS profile.

After the analysis of the Fe/Ni multilayers was completed, the same steps were taken in characterizing the behavior of the Ti/Nb film. The slope of the composition graph was calculated in atomic percent per nanometer for the Ti intermixing into the Nb layer and for the Nb intermixing into the Ti layer for the STEM-EELS profile. These two slopes were then expressed as a ratio in order to indentify any differences in the elemental interfacial behavior across the techniques. This result, depicted in Table 4.1, shows that for the STEM-EELS compositional profile for Ti/Nb, the ratio of the compositional gradients is 1.33. This result was used as a reference for comparison of later analysis of the perpendicular APT characterization technique.

This measurement was performed in the same manner for the data collected from the perpendicularly oriented APT geometry. The results of these calculations, displayed in Table 4.1, show that for the Ti/Nb films in the perpendicular geometry, the ratio of the Ti on Nb to Nb on Ti was 0.926—a 30.37% deviation from the reference EELS profile. This value shows that not only does the layer thicknesses measured from the APT analysis deviate from the STEM-EELS profile, the behavior at the interface is also affected.

4.2.2 Correlation between parallel APT and EELS

All of the elemental modulation layer spacings had discrepancies with its characterized counterparts, as seen in Table 3.1. In both the Fe/Ni and Ti/Nb, the reconstructed atom maps from the parallel limiting geometry, there is a local magnification that is occurring within the

layer with the greater elemental evaporation field, the Ni and the Nb. This is due to the requirements for evaporation at the intermixed interfaces of these specimens. As a consequence of this varied evaporation field at the interface of the parallel orientation, the tip end form evolves to compensate for these evaporation requirement differences – this is evident by the local curvatures that form in the tip. A TEM micrograph of the Ti/Nb tip, which has been evaporated for over five million ions, is seen in Figure 4.1(b). Clearly, it is evident that a ‘hump’ like morphology has formed at the tip at the interface of the layers. This generates a local curvature, which varies from the global curvature used for the reconstruction. In addition, this change in local curvature deviates from the assumption on which the current reconstruction algorithms are created—a single or constant radius of curvature. In this case, artifacts are generated because the reconstruction software available did not adequately account for the actual tip shape in this limiting geometry.

This deviation in local curvature, or humping, is not as prevalent in the Fe/Ni atom probe tip, as shown in Figure 4.1(a). This is due to the fact that the elemental evaporation fields of the two species are much closer together, leading to a more similar field strength needed for evaporation to occur. This decreases the amount of local magnification that is seen within the reconstruction, using similar reconstruction parameters. As Schmitz discussed in detail, these local humps produce local magnifications, which produce ion trajectories that can spread or compress the data spatially under a single radius of curvature assumption [22].

This difference in reconstructed layer thickness, however, does not mean that the composition at the interface is altered due to the evaporation experiment. The next step in the analysis involved examining what was occurring at the interface of these two different systems across the two remaining techniques (STEM-EELS and APT in the parallel geometry) in order to

fully answer the question that motivated this research. In order to perform this analysis, compositional gradients were calculated for these techniques across each separate layer interface. Essentially, the slope of the composition graph was calculated in atomic percent per nanometer for the Fe intermixing into the Ni layer and for the Ni intermixing into the Fe layer for the STEM-EELS profile. These two slopes were then expressed as a ratio in order to identify any differences in interfacial behavior across the techniques. This result, depicted in Table 4.1, shows that for the STEM-EELS compositional profile for Fe/Ni, the ratio of the compositional gradients is 1.0, identical to the gradient laid out above. This result was used as a reference for comparison of later analysis of the parallel APT characterization technique.

This measurement was performed in the same manner for the data collected from the atom probe data set collected in the parallel orientation. The results of these calculations, displayed in Table 4.1, show that for the parallel geometry, the compositional gradient ratio of the Fe on Ni to Ni on Fe was calculated to be 1.085—an 8.5% deviation from the reference EELS profile. These numbers show that while the average layer thickness for the parallel orientation deviated from that of the STEM-EELS data, the behavior at the interface is relatively similar.

After the analysis of the Fe/Ni multilayers was completed, the same steps were taken in characterizing the behavior of the Ti/Nb film. The slope of the composition graph was calculated in atomic percent per nanometer for the Ti intermixing into the Nb layer and for the Nb intermixing into the Ti layer for the STEM-EELS profile. These two slopes were then expressed as a ratio in order to indentify any differences in interfacial behavior across the techniques. This result, depicted in Table 4.1, shows that for the STEM-EELS compositional profile for Ti/Nb, the ratio of the compositional gradients is 1.33. This result was used as a

reference for comparison of later analysis of the parallel orientation within the evaporation experiment.

This measurement was performed in the same manner for the data collected in the parallel evaporation orientation. For this parallel geometry, the compositional gradient ratio of the Ti on Nb to Nb on Ti was calculated to be 1.453—a 9.3% deviation from the reference EELS profile. This value shows that although the layer thicknesses measured from the APT analysis may have deviated from the STEM-EELS profile, but the behavior at the interface is relatively similar. This is a stark contrast to the findings within the Fe/Ni system.

4.2.3 Correlation between perpendicular and parallel APT

It is evident from looking at the data in Table 4.1 that there are differences, not only in layer thickness, but also in the compositional profiles across the interfaces of the films in the two limiting geometries. In the case involving two materials of similar evaporation fields, Fe and Ni in this set of experiments, it was found that the Ni elemental layer thicknesses were close in both of the limiting geometries, but the layer thickness was closer in the perpendicular orientation. For the Fe layers, the perpendicular atom probe orientation was a close match to the layer thickness calculated from the EELS profile. The Fe layer thickness in the parallel orientation was almost double the recorded thickness from the EELS profile. The layer thickness was not the only feature of interest when determining if artifacts were present and if present, how severe they were. The ratio of the compositions in and out of the interfaces for the perpendicular orientation was only in deviation of 0.8% from the EELS profile. The parallel limiting geometry, however, exhibited a deviation of 8.5% from the EELS profile. Therefore, for the case of two materials with similar elemental evaporation fields, the compositional profiles across

the interfaces do not have severe reconstruction artifacts, although the perpendicular orientation has less severe artifacts. The layer thicknesses are a much closer match in the perpendicular evaporation orientation.

For the case of two materials with vastly different elemental evaporation fields, Ti and Nb in this set of experiments, it was found that both elements in both orientations deviated from the layer thicknesses observed in the EELS data sets. The Ti layer in the perpendicular evaporation orientation was almost identical to the layer thickness observed in the EELS compositional profiles. In the parallel orientation for Ti, however, the observed layer thickness was about two-and-a-half times smaller than the layers observed in the EELS profile, as displayed in Table 4.1. The Nb layers, unlike the Ti, exhibited issues in both the parallel and perpendicular evaporation orientations. In the case of the parallel orientation, the Nb layer is almost one-and-a-half times thicker than the Nb layer observed in the EELS profile. In the case of the perpendicular orientation, the deviation is less severe, although it still exists. The Nb layer thickness in this orientation was measured to be 1.97 nm, while the measured layer thickness in the EELS profile was 3.60 nm. As for the compositional behavior at the interface of these two layers, there is a deviation from the EELS profile in both the parallel and perpendicular orientations.

It is therefore observed that orienting the specimen so that materials with vastly different elemental evaporation fields are able to evaporate simultaneously may increase the length of the atom probe run, but it does not eliminate the reconstruction artifacts, if anything this orientation may make reconstruction issues worse. The ratio of the compositions across the interfaces was closer to the actual specimen in this parallel orientation, but the bilayer thickness was more distorted in this orientation. This is evidence that the preferential evaporation played less of a

role in the reconstruction, but the local magnification effect from the different layers caused artifacts in the atom maps.

4.3 Reconstruction Artifacts Explained by Tip Shape Evolution

In general, atom probe reconstruction algorithms assume a constant evaporation field across the surface of the specimen. In reality, during experimental field evaporation through the specimen interfaces, chemical inhomogeneity modulates the evaporation field at the surface, causing a non-hemispherical tip with curvature variation to form [45]. In order to determine how much of an affect these curvature variations would have on the reconstructions, the severity of the curvature variations as a function of evaporation field differences needed to be identified. Figure 4.1, shows the difference in local curvature between a material with similar evaporation fields, Fe/Ni with evaporation fields of 33 V/nm and 35 V/nm, in Figure 4.1(a) and a material with very dissimilar evaporation fields, Ti/Nb with evaporation fields of 28 V/nm and 37 V/nm, in Figure 4.1(b) [9]. Both of the TEM micrographs shown in the figure were acquired using bright field imaging.

Since this specimen contains elements that consist of two different evaporation fields, the energetic need for these two to field evaporate is different. This difference leads to the creation of surface modulations at each of the layer interfaces. When an atom is evaporated at one of these interfaces, not only will it be accelerated towards the detector from the evaporation event, but it will be repelled at some angle due to the local curvature within the tip.

Currently, there are very few reports on how to correct for local curvature during reconstruction [38, 45]. This artifact is difficult to correct with a basic algorithm since it affects each materials system in a different manner. In Figure 4.1(a), the tip shape of a Fe/Ni film is

shown. The evaporation field strengths of these two elements are close together, 33 and 35 V/nm, respectively [9]. This image shows that due to the similar field strengths, there is much less severe, if any, radius of curvature modulation at the layer interfaces. This is due to little difference in the evaporation field strengths of the two elements, leading to much less preferential evaporation from the intermixed interfaces. This lack of preferential evaporation allows the main factor in flight path to be the evaporation event, leading to reconstructed data sets with fewer reconstruction artifacts. Understanding not only the onset, but also the severity of these deviations from a constant radius of curvature in different material systems is the first step in being able to develop materials system specific reconstruction algorithms to rectify any reconstruction artifacts [4].

4.4 TipSim Evaporation Simulations

The TipSim software was used to simulate field evaporation for the two different material systems, Fe/Ni and Ti/Nb, in the two limiting geometries, parallel and perpendicular. Initially, there were 10,000 ions that were ‘fast evaporated’ in order to start the process, followed by 50,000 ions evaporated in 100 ion steps, to allow for tip shape evolution. Within the simulation, the conditions within the LEAP chamber were held at a temperature of 1 K and a pressure of 10^{-13} Torr. The target pulse fraction was 0.15, and the flight path was held at 90 mm.

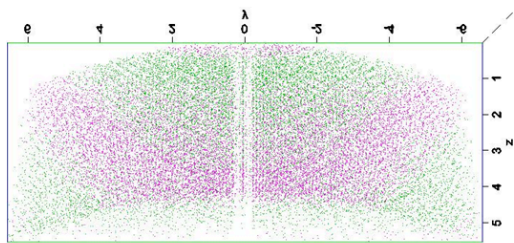
After the simulations were complete, as with actual atom probe data, the reconstruction parameters needed to be optimized in order to properly interpret the data. In order to make this optimization process more straight forward, the determined k-factor and image compression factor for these materials systems were kept the same as the actual data. In order to alter the reconstruction parameters in order to optimize the fit of the digital atom maps to the actual

specimens, the initial radius of the tip and the estimated shank half angle were altered within the reconstruction software. This was completed by systematically changing the radius and calculating the corresponding shank angle and qualitatively analyzing the resulting tip shape. The main features of interest within the reconstructions after these values were changed were the thicknesses of the respective layers, the curvature of the deposited layers, and the overall shape of the specimen tip. This was completed for both of the material systems in both of the limiting geometries.

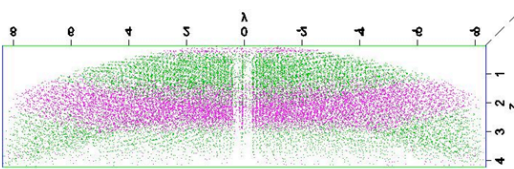
As expected, each of the limiting geometries in each of the material systems had its own ideal set of reconstruction parameters due to different elemental evaporation fields and different evaporation orientations. In Figure 4.2, the reconstruction of the perpendicular orientation of the Fe/Ni multilayered film is shown. The initial radius, and the computed half shank angle, were altered in order to optimize the planar nature of the layers as well as the thickness of the layers. Figure 4.3 shows this same process being utilized for the parallel orientation of the Fe/Ni system. It is evident in this figure that the most sensitive aspect of the parallel reconstruction is the thickness of the multilayers, while in the previous figure, the planar nature of these layers was the most sensitive aspect of the reconstruction. Figure 4.4 and Figure 4.5 show the reconstructions for different applied radii and computed half shank angles for the Ti/Nb perpendicular and parallel systems, respectively. These atom maps display the same behavior as the Fe/Ni systems. The perpendicular system's planar interfaces are most affected by changing the reconstruction parameters, and the parallel system's layer thicknesses are the most affected by changing the reconstruction parameters.

It is visually evident in both the Fe/Ni and Ti/Nb systems above, Figure 4.2, Figure 4.3, Figure 4.4 and Figure 4.5, that there is a stark deviance from the experimental atom maps found

a)



b)



c)

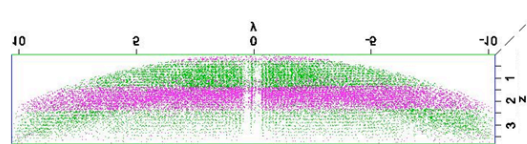


Figure 4.2 TipSim Fe/Ni Reconstruction in the Perpendicular Orientation
All measurements shown are in nm

- a) Under Estimated Initial Radius (15 nm) – Fe (Pink), Ni (Green)
- b) Best Estimation of Initial Radius (20 nm) – Fe (Pink), Ni (Green)
- c) Over Estimated Initial Radius (25 nm) – Fe (Pink), Ni (Green)

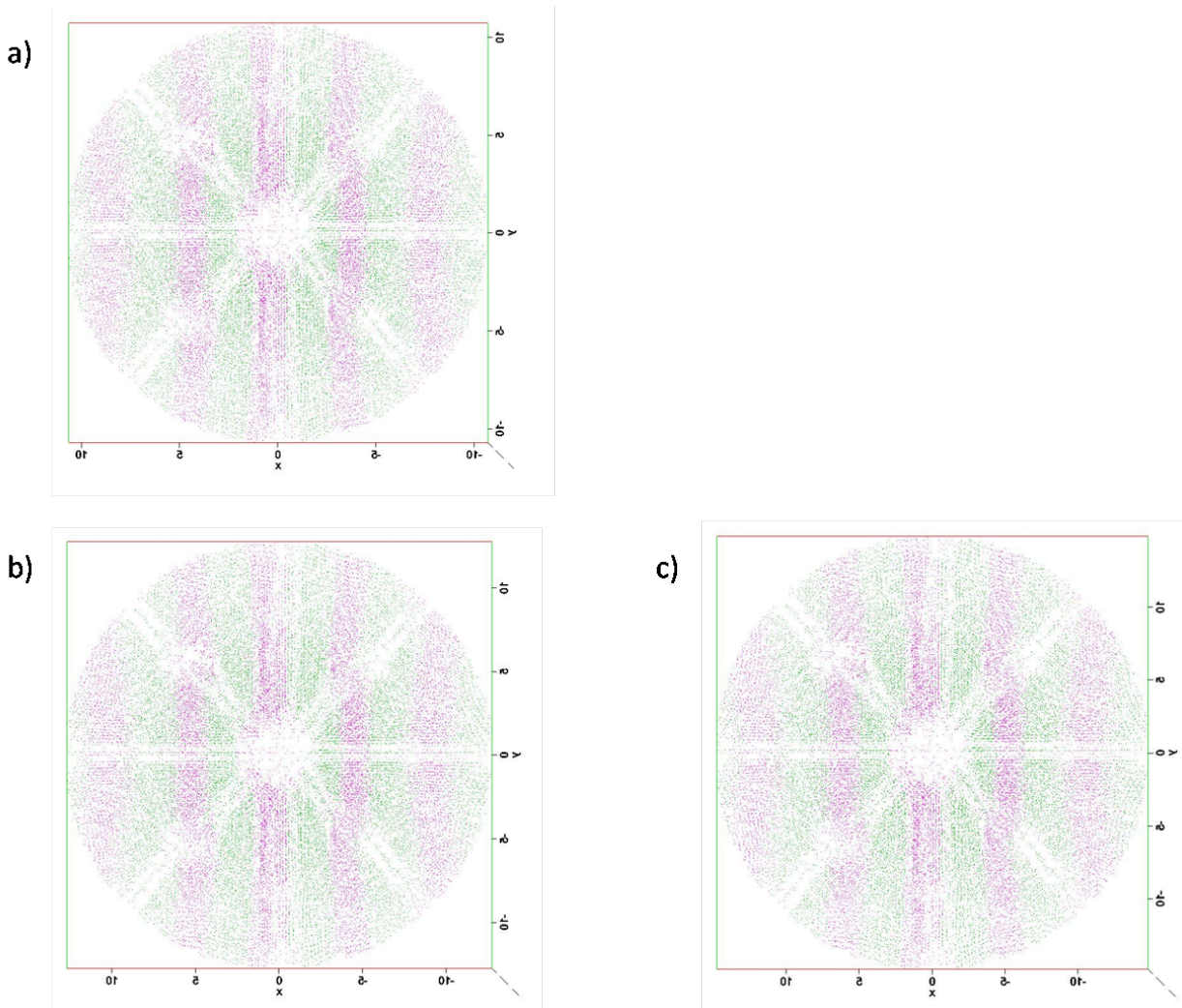


Figure 4.3 TipSim Fe/Ni Reconstruction in the Parallel Orientation

All measurements shown are in nm

- a) Under Estimated Initial Radius (25 nm) – Fe (Pink), Ni (Green)
- b) Best Estimation of Initial Radius (30 nm) – Fe (Pink), Ni (Green)
- c) Over Estimated Initial Radius (35 nm) – Fe (Pink), Ni (Green)

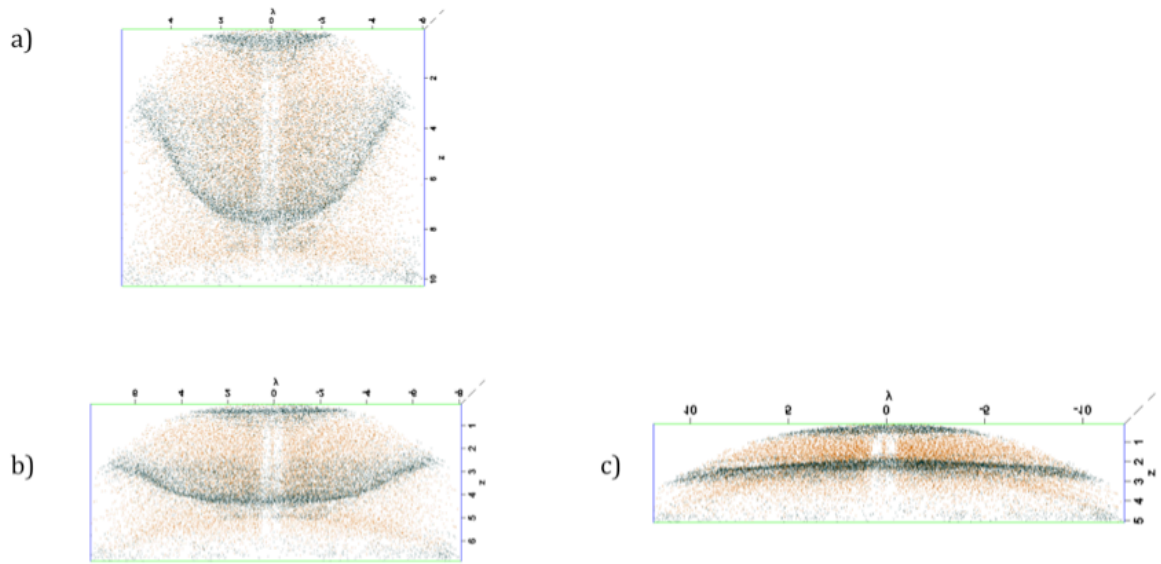


Figure 4.4 TipSim Ti/Nb Reconstruction in the Perpendicular Orientation
All measurements shown are in nm

- a) Reconstructed with an Initial Tip Radius of 7.5 nm
- b) Reconstructed with an Initial Tip Radius of 10 nm
- c) Reconstructed with an Initial Tip Radius of 15 nm

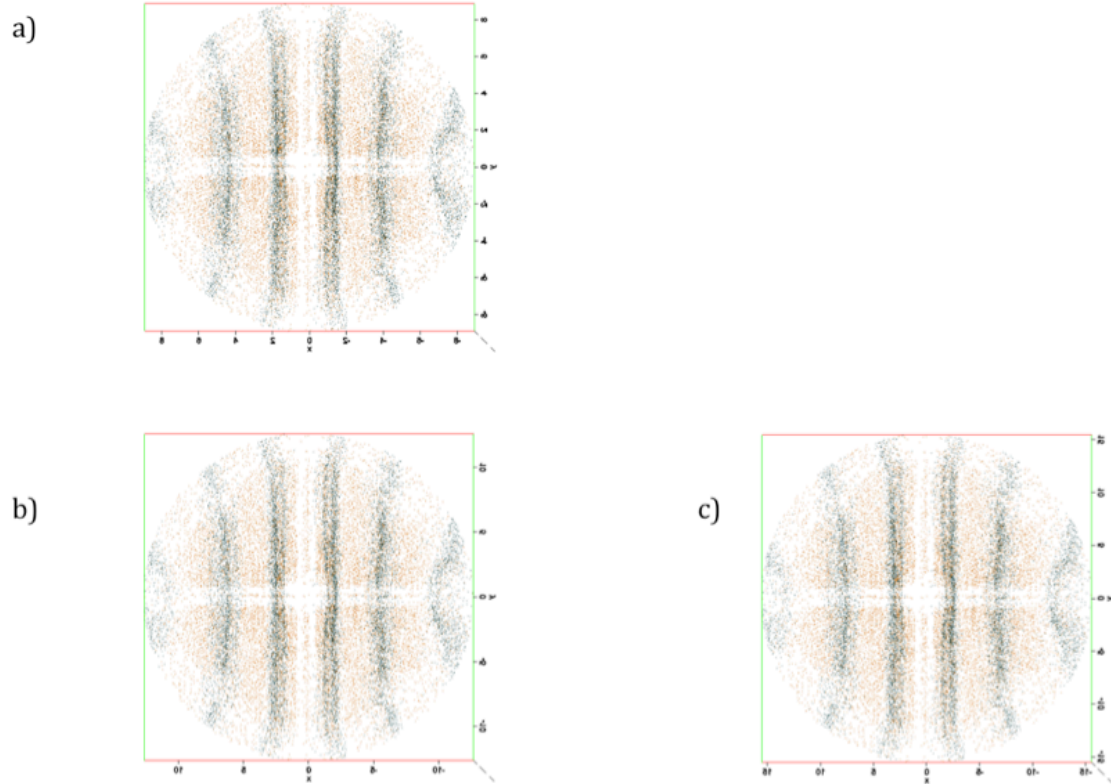


Figure 4.5 TipSim Ti/Nb Reconstruction in the Parallel Orientation

All measurements shown are in nm

- a) Reconstructed with an Initial Tip Radius of 20 nm
- b) Reconstructed with an Initial Tip Radius of 28.5 nm
- c) Reconstructed with an Initial Tip Radius of 35 nm

in Figure 3.8 and Figure 3.14. This is because while the TipSim program provides a nice reconstruction of a generated atom probe specimen, it does not fully predict any issues or sources of artifacts from the elemental combination within a material system. As shown in the experimental atom maps, there are local magnification effects, evaporation issues from elemental layer intermixing, and environmental contamination within the experimental data sets. This simulation software falls short in predicting these aspects of the evaporation experiment. Identifying artifacts within a reconstruction is still left completely to the user.

4.5 Ion milling damage

Since the APT specimens were lifted-out and sharpened using a dual-beam FIB, one of the concerns was insuring that Ga damage did not influence the integrity of the layer interfaces. Early on in the stages of this research, there were some atom probe specimens that were overly exposed to Ga implantation. Not knowing of the problem that had been created in the FIB, these tips were characterized in an atom probe. Upon reconstruction of the evaporation experiments, it was evident that the extent of intermixing varied with the orientation of the elemental interfaces. The specimens prepared in the perpendicular orientation were transformed into a nearly a solid solution of Fe and Ni within the film. In the parallel orientation, the specimens that were exposed to an excessive amount of gallium implantation still exhibited a somewhat layered formation. This is because in the perpendicular orientation, the different elements, when bombarded with Ga ions, were displaced into each other. In the parallel orientation, with the ion beam orientated normal to the specimen apex, the displaced atoms were displaced deeper into their own layers. In the perpendicular orientation, the Ga ions strike perpendicular to the layer interfaces, as shown in Figure 6(a). In the parallel orientation, there is a channeling effect that

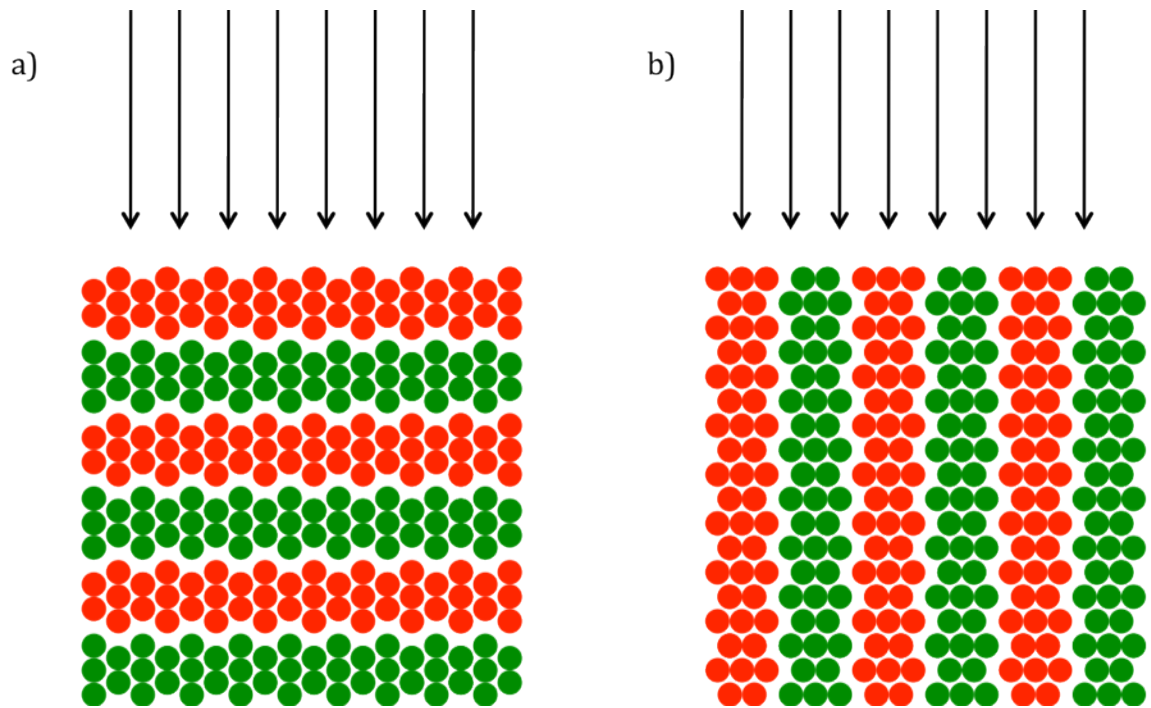


Figure 4.6 Orientation Dependent Ga Ion Beam Damage

- a) Perpendicular Preparation Orientation
- b) Parallel Preparation Orientation

allows the atoms to stay within their own layers, as shown in Figure 6(b). The migration of the Ga in these reconstructed atom maps is shown in Figure 4.7(a) and Figure 4.7(b), respectively. SRIM simulations were employed in order to simulate the effect that certain levels of Ga damage would have on the multilayered thin films in the two different orientations.

The Kinetic Monte Carlo make-up of these simulations allow for the characterization of the amount of damage that could be included during preparation in a dual-beam FIB. These simulations were executed for the four different specimen preparation methods found in this research: Fe/Ni multilayered thin film in the perpendicular orientation, Fe/Ni multilayered thin film in the parallel orientation, Ti/Nb multilayered thin film in the perpendicular orientation, and Ti/Nb multilayered thin film in the parallel orientation. Twenty elemental layers were generated, and the elemental information for these films was uploaded from within the software. The densities of the Fe, Ni, Ti, and Nb were 7.8658 g/cm^3 , 8.8955 g/cm^3 , 4.5189 g/cm^3 , and 8.57 g/cm^3 , respectively. 100,000 gallium ions were allowed to strike the surface, after being accelerated at an intrinsic voltage of 30 keV, similar to that used during sample preparation in the dual-beam FIB.

The SRIM simulation software was able to output the gallium ion trajectories within the thin films, the number of vacancies produced, the energy to the recoils (damage), and the ionization distribution. Each of these plots show regions in which the APT specimens will exhibit behavior dissimilar to that of the rest of the film. By knowing this information, the accelerating voltage and exposure to the ion beam can be limited, in addition to only examining APT data collected after a certain number of ions were allowed to evaporate, essentially throwing-away any biased data. In Figure 4.8 below, the ion trajectories in the XY axis are shown for the Fe/Ni parallel and perpendicular geometries as well as for the Ti/Nb parallel and

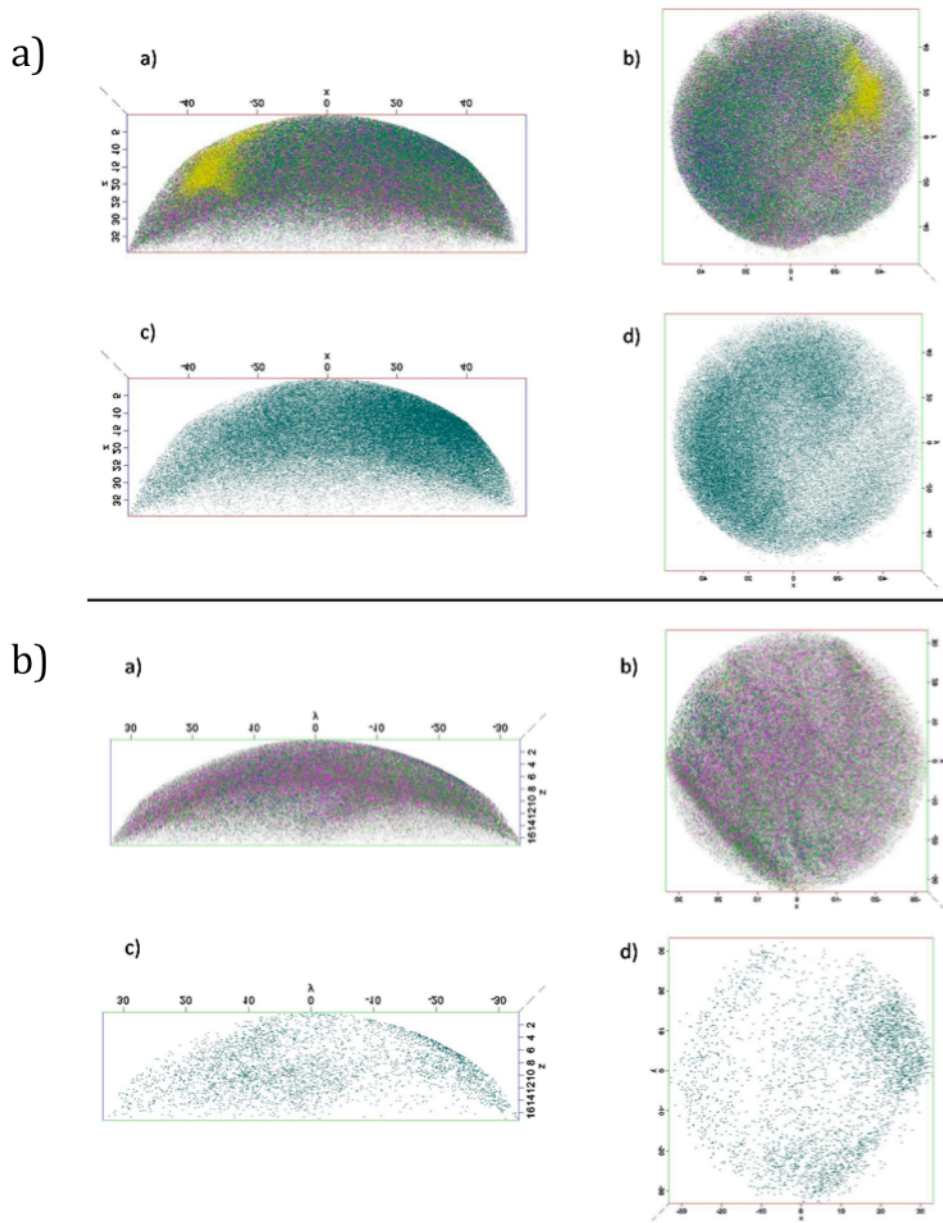


Figure 4.7 APT Reconstructed Atom Maps with Gallium Damage

- a) Perpendicular Orientation
 - a. Lateral View – Fe (Pink), Ni (Green), H (Yellow), Ga (Blue)
 - b. Top View – Fe (Pink), Ni (Green), H (Yellow), Ga (Blue)
 - c. Lateral View – Ga only
 - d. Top View – Ga only
- b) Parallel Orientation
 - a. Lateral View – Fe (Pink), Ni (Green), H (Yellow), Ga (Blue)
 - b. Top View – Fe (Pink), Ni (Green), H (Yellow), Ga (Blue)
 - c. Lateral View – Ga only
 - d. Top View – Ga only

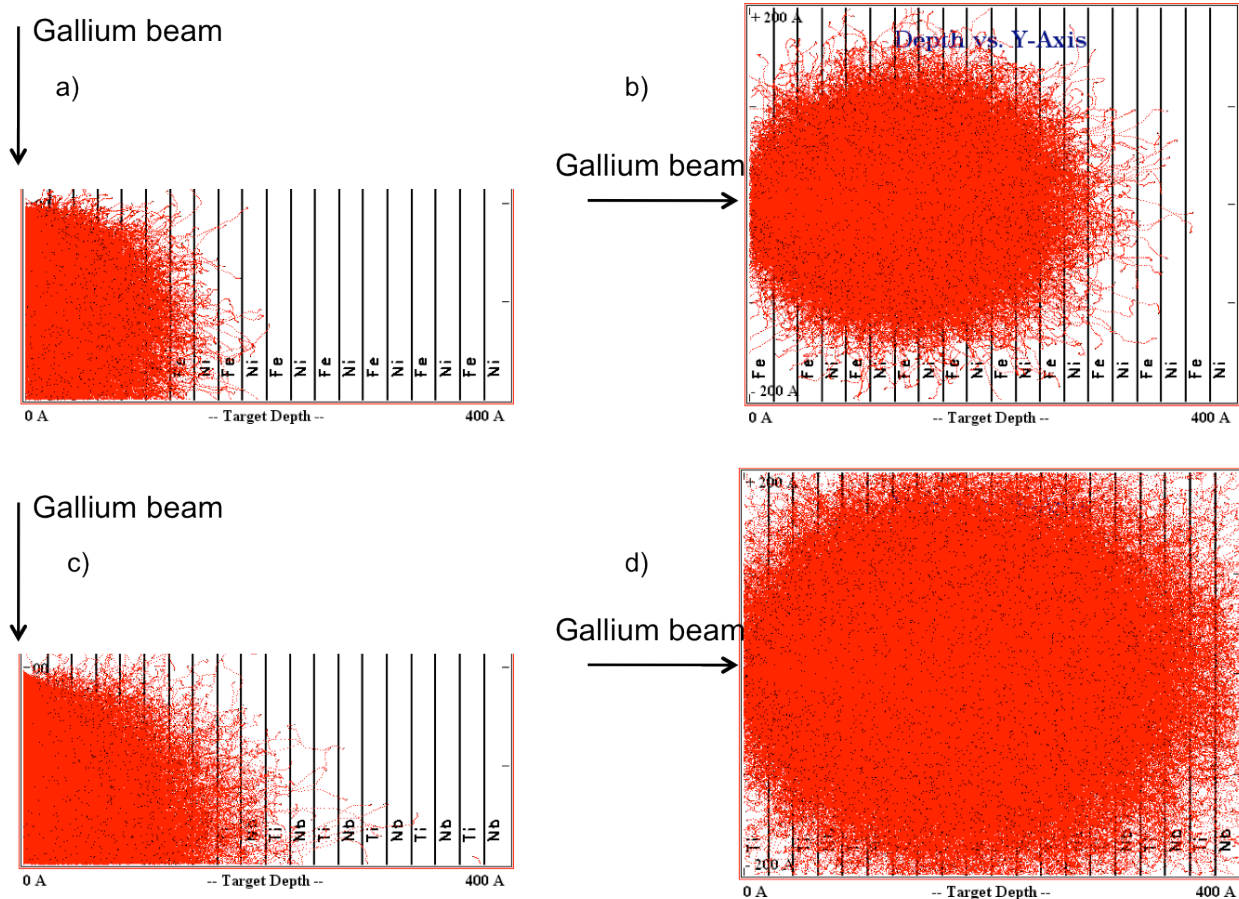


Figure 4.8 SRIM Simulations – Ion Trajectories

- a) Fe/Ni in the Parallel Orientation
- b) Fe/Ni in the Perpendicular Orientation
- c) Ti/Nb in the Parallel Orientation
- d) Ti/Nb in the Perpendicular Orientation

perpendicular geometries. Figure 4.9 shows the collision events within these ranges as a function of target depth and also shows the number of gallium atoms that displaced previously sputtered atoms and thus produced vacancies within the films.

These simulations were then performed for the perpendicular limiting geometry in both materials systems with a protective platinum cap with a thickness of 1 μm deposited directly on the surface of the multilayered thin films. This was done to simulate the degree of gallium damage and implantation an actual specimen can experience when being prepared in a dual-beam FIB. This actual platinum thickness was chosen since this is the procedure used to create the atom probe specimens. The density of the Pt in this simulation software was 21.45 g/cm³, and once again, 100,000 gallium ions were allowed to strike the surface with an accelerating voltage of 30 keV. In Figure 4.10, the ion trajectories in the XY axis are shown for the Fe/Ni perpendicular geometry as well as for the Ti/Nb perpendicular geometry. Figure 4.11 shows the collision events within these ranges as a function of the target depth and the number of vacancies produced within the film.

In order to demonstrate what types of damage would be seen in actual practice, the simulations were repeated with a 1 μm Pt protective cap, as is actually used when preparing samples using a FIB. These results, shown in Figure 4.10 and Figure 4.11, depict a system with much less Ga damage and implantation. Since this is most similar to the systems used for experimentation, these models are used in order to interpret collected atom probe data. When reconstructing the collected data, the first million ions were left out of the analysis in order to discard any of the atoms that may have been displaced due to gallium damage. Mostly, after these first million ions were discarded, the amount of Ga observed in the specimens was less than 2%.

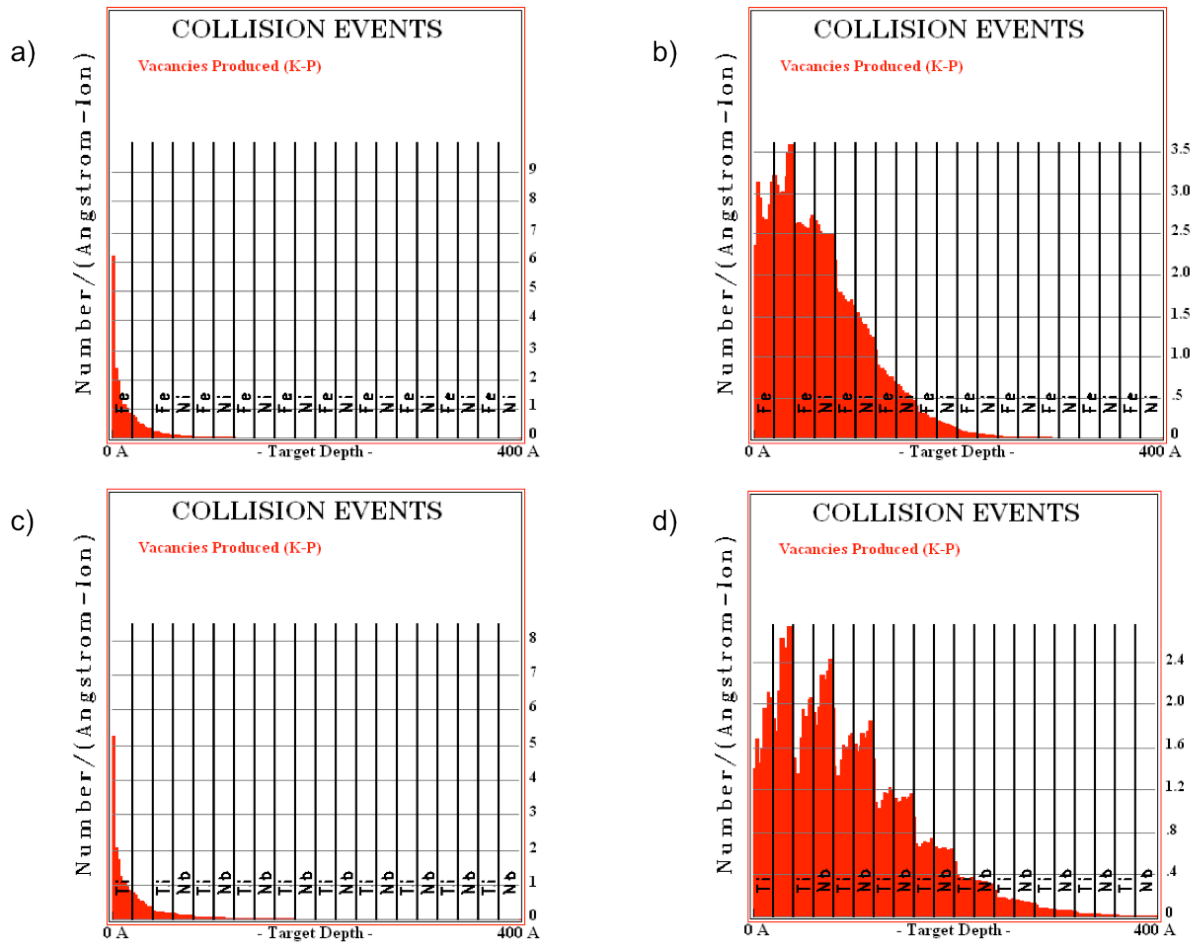


Figure 4.9 SRIM Simulations – Collision Events

- Fe/Ni in the Parallel Orientation
- Fe/Ni in the Perpendicular Orientation
- Ti/Nb in the Parallel Orientation
- Ti/Nb in the Perpendicular Orientation

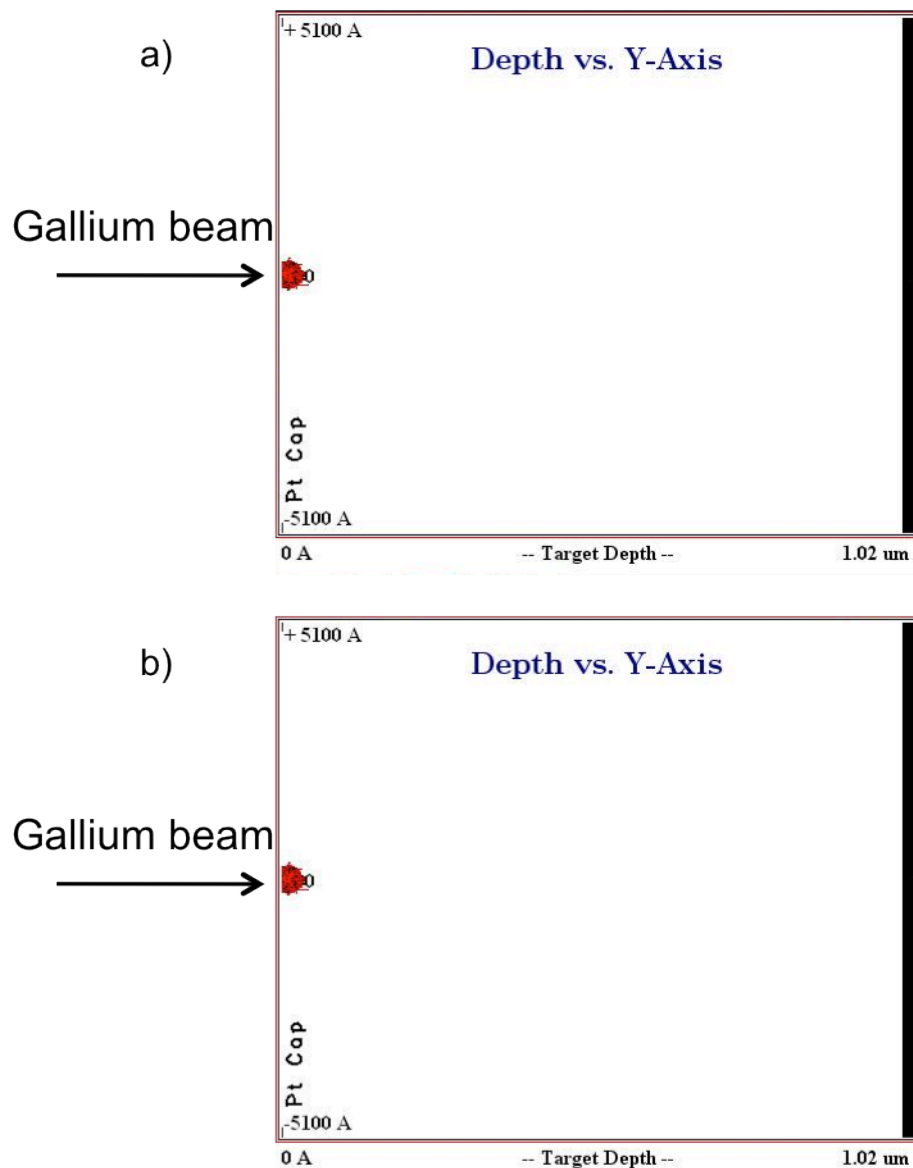


Figure 4.10 SRIM Simulations with Platinum Cap – Ion Trajectories

- a) Fe/Ni Multilayered Thin Films in the Perpendicular Orientation
- b) Ti/Nb Multilayered Thin Films in the Perpendicular Orientation

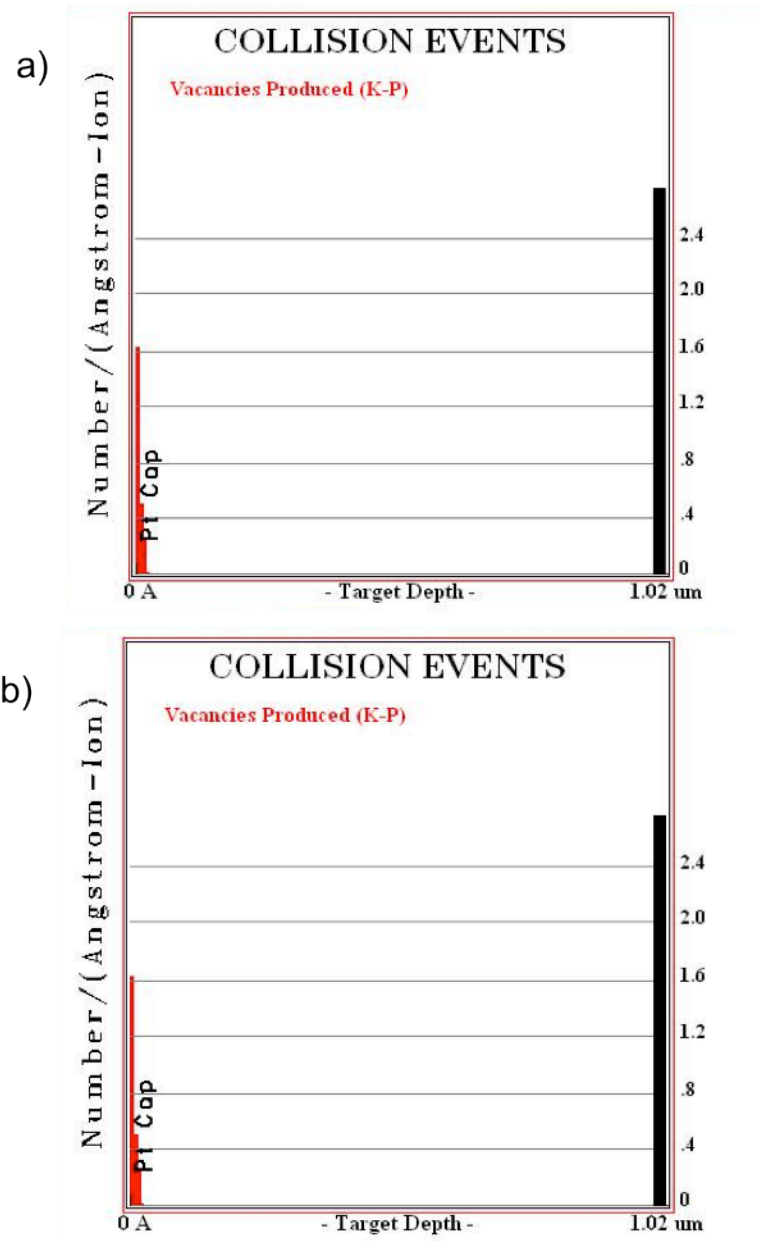


Figure 4.11 SRIM Simulations with Platinum Cap – Collision Events

- a) Fe/Ni Multilayered Thin Film in Perpendicular Orientation
- b) Ti/Nb Multilayered Thin Film in Perpendicular Orientation

The protective Pt cap was not the only helpful realization that came from these simulations. From both initial inexperienced experimentation results which were then backed by SRIM simulation results, it was found that the specimens prepared in the parallel limiting geometry exhibited less damage when exposed to a Ga ion beam, as shown in Figure 4.10 and Figure 4.11. As in most materials, there is still Ga damage present, but instead of pushing Fe atoms into the Ni layers and Ni atoms into the Fe layers, the Fe atoms were pushed further into the Fe layers, and the Ni atoms were pushed further into the Ni layers. While this still alters the reconstruction from the actual system, it is much less severe than intermixing. If an experiment were being completed in order to understand the behavior of a system at the atomic scale, this orientation would still leave the layers somewhat intact. This would allow the researcher to infer general information about the microstructure of the system, even if the user was not careful or experienced in using an ion beam. Upon perfection of the technique, the information inferred from the damage atom maps could be verified in a form that allows for compositional quantification.

CHAPTER 5

CONCLUSION AND FUTURE WORK

When a field evaporation experiment exposes a new layer at the apex of the surface, is the measured composition at the interface, via the current reconstruction algorithms, significantly altered due to these differences in the evaporation fields? This work was completed in order to address this question by an identification of reconstruction issues, such as preferential evaporation and local magnification, and how their severity varies as a function of material selection as well as the orientation of the specimen interfaces. The motivation for the research outlined in this thesis was to determine if changing the orientation of the interfaces within a specimen would alter the severity and occurrence of these reconstruction artifacts. The completed work presented data and specimen preparation methods for two different bilayered material systems. These two films were specifically chosen because within the Fe/Ni film, there is very little difference between the elemental evaporation fields of iron and nickel, and within the Ti/Nb film, there is a stark contrast between the elemental evaporation fields of titanium and niobium.

These two films were examined in the traditional orientation and in the parallel orientation proposed by Lawrence *et al.* [6]. In order to be able to confidently identify the occurrence and severity of reconstruction artifacts in these cases, cross-correlation microscopy was employed between APT and EELS to quantify what the actual atomic behavior was within the specimen. Some of these types included cross-correlation of shape, volume fraction, and chemical composition. In this research, the goal was to identify the local magnification effects and preferential evaporation at the interfaces, so chemical composition cross-correlation needed

to be used. The most ideal technique to compare the chemical make-up of the samples through the interfaces to that reported by atom probe was EELS. By utilizing the average elemental layer thickness from all three techniques, as well as the compositional gradients across the separate interfaces, artifact identification and characterization could be completed. Though similar issues, such as local magnification reconstruction issues and associated effects due to the orientation of the APT tips have been addressed, this work strived to provide a systematic study of the same materials in these two limiting geometries, in order to be able to quantify the extent of these artifacts as a function differences in field strength and orientation. The results were then compared to an independent STEM EELS profile to determine the fidelity of the atom probe reconstruction.

It was determined that the film with similar elemental evaporation fields, the Fe/Ni multilayered film, had measured layer thicknesses for the APT analysis that slightly deviated from the reference STEM-EELS thickness, but the behavior of the compositional gradients at the interfaces had little deviation from the reference ratio, in atomic percent per nanometer. The film with elemental evaporation fields that inherently have a deviation from each other, the Ti/Nb multilayered film, had measured layer thicknesses for the APT analysis that deviated from the reference STEM-EELS reference. In the perpendicular evaporation orientation, the behavior of the compositional gradient at the interface had a measureable deviation from the reference profile. However, in the parallel evaporation orientation, the behavior of the compositional gradient at the interface had a less severe deviation from the reference STEM-EELS profile. This is believed to exist because in general, atom probe reconstruction algorithms assume a constant evaporation field across the surface of the specimen. In this case, especially for the Ti/Nb film, as the analysis progresses through the specimen interface, chemical inhomogeneity

modulates the evaporation field at the specimen surface, causing a non-hemispherical cap with a curvature variation to form [45]. This deviation from the quantification assumption introduced reconstruction artifacts, thus degrading the spatial resolution of the APT technique for materials containing elements with vastly different evaporation fields.

In a much broader sense, what was learned in this study was that orienting the interface between two different materials, whether they have similar elemental evaporation fields or vastly different elemental evaporation fields, parallel to the evaporation direction allows for evaporation experiments in an atom probe that will last for a greater number of collected ions. In materials with vastly different evaporation fields, this orientation will have reconstruction artifacts that are less severe than those encountered in the traditional perpendicular orientation. The trade-off for this decrease in reconstruction artifacts, though, is the spatial resolution of the tool. In the plane containing the interface between the two materials, the resolution is decreased by a factor of ten, from 0.05 nm in the perpendicular orientation to 0.5 nm in the parallel orientation. Additionally, in systems containing materials with very similar elemental evaporation fields, this parallel orientation created reconstruction artifacts in the thickness of the layers due to the local magnification effects from the two different materials evaporating simultaneously. However, when analyzing the compositional gradient across the interface between the two materials, the deviation from the specimen standard was mild. This parallel orientation proposed by Lawrence *et al.* provides an experiment that is much easier to perform while diminishing the reconstruction artifacts found in material systems with vastly different evaporation fields, which normally generate artifacts when evaporated in the perpendicular orientation [6]. This orientation, though, does not have as large of a payoff for material systems with similar evaporation fields.

Recommended work for a future researcher wishing to continue this set of experiments would be to investigate the behavior of interface orientation in ‘bulk’ materials, not thin films. Specifically orienting grain boundaries and lathes within an atom probe specimen could allow for more successful evaporation experiments and easier to identify compositional gradients. In addition, if the future researcher were perusing a modeling approach, developing a more in-depth simulation of the evaporation experiment would be an invaluable addition to the field. If it were possible to visualize and characterize reconstruction artifacts on a theoretical level, it would then be possible to write new algorithms to correct these issues in the actual specimens. This, along with cross-correlation microscopy, would allow for the generation of reconstructions that represent the true atomic positions within a prepared specimen.

CHAPTER 6

REFERENCES

1. Miller, M.K., A. Cerezo, M.G. Hetherington, G.D.W. Smith. Atom Probe Field Ion Microscopy. Oxford University Press, Oxford. 1996.
2. Danoix, F. T, Gloriant, T. Epicier, F. Vurpillot, and W. Lefebvre. "Atom Probe Field Ion Microscopy and High Resolution Electron Microscopy." *INVC and IFES 2006-Technical Digest-19th International International Vacuum Nanoelectronics Conference and 50th International Field Emission Symposium* (2006) 517.
3. Marquis, E.A. and J.M. Hyde. "Applications of Atom-Probe Tomography to the Characterization of Solute Behaviours." *Materials Science and Engineering R: Reports* 69 (2010) 37-62.
4. Larson, D. J., T. J. Prosa, B. P. Geiser, and W. F. Egelhoff, Jr. "Effect of Analysis Direction on the Measurement of Interfacial Mixing in Thin Metal Layers with Atom Probe Tomography." *Ultramicroscopy IFES 2010* (2010). Print.
5. Miller, M.K., and R.G. Forbes. "Atom Probe Tomography." *Materials Characterization* 60 (2009): 461-69. *Science Direct*. Web.
6. D. Lawrence, R. Alvis, D. Olson. "Specimen Preparation for Cross-Section Atom Probe Analysis." *Microscopy Microanalysis* 14 (2008)
7. A. Genc, R. Banerjee, G.B. Thompson, D.M. Maher, A.W. Johnson, H.L. Fraser. "Complementary Techniques for the Characterization of Thin Film Ti/Nb Multilayers."
8. Arslan, I., E.A. Marquis, M. Homer, M.A. Hekmaty, N.C. Bartlett. "Towards Better 3-D Reconstructions by Combining Electron Tomography and Atom-Probe Tomography." *Ultramicroscopy*. 108 (2008): 1579-1585.
9. Tsong, T.T. *Surface Science*. 70 (1978) 211.
10. Lang, Ch, and G. Schmitz. "Microstructure-controlled Interdiffusion of Cu/Co/Au Thin Films Investigated by Three-dimensional Atom Probe." *Materials Science and Engineering A* 353.1-2 (2003): 119-25. Print.
11. G.B. Thompson, M.K. Miller, H.L. Fraser. "Some Aspects of Atom Probe Specimen Preparation and Analysis of Thin Film Materials." *Ultramicroscopy*, 100 (2004) 25-34.
12. Hono, K., Y. Maeda, J. Li, and T. Sakurai. "Atom Probe Analysis of Sputtered Co-Cr Magnetic Thin Films." *Applied Surface Science* 67.1-4 (1993): 386-90. Print.

13. Teng, Mao-Ying, Chun-Yu Hsu, Kuo-Shung Liu, and I-Nan Lin. "Effect of Si Dielectric Materials on the Magnetic Coupling of Tb-Fe-Co Multilayer Thin Films." *Journal of Magnetism and Magnetic Materials* 239 (2002): 338-42. Print.
14. Zhang, F., Z. Huang, Z. Lan, Z. Cui, J. Guo, W. Cheng, and X. Yang. "Effect of Chromium Interlayer on Magnetic Exchange Coupling of SmCo/Cr/TbFeCo Multilayer Thin Films." *Journal of Rare Earths* 26.3 (2008): 375-77. *Science Direct*. Web.
15. Vovk, V., G. Schmitz, and R. Kirchheim. "Three-dimensional Atom Probe Investigation of Co/Al Thin Film Reaction." *Microelectronic Engineering* 70.2-4 (2003): 533-38. Print.
16. Thompson, K., D. J. Larson, R. M. Ulfig, J. H. Bunton, and T. F. Kelly. "Analyzing Si-based Structures in 3D with a Laser-Pulsed Local Electrode Atom Probe." *Solid State Technology* 49.6 (2006): 65. Print.
17. Muller, E.W., J.P. Panitz, S.B. McClane. "The Atom Probe Field Ion Microscope." *Review of Scientific Instruments* 39 (1968): 83-6.
18. Kellogg, G.L., T.T. Tsong. "Pulser-Laser Atom-Probe Field-Ion Microscopy." *Journal of Applied Physics* 51 (1980): 1184-93.
19. Miller, M.K. Atom Probe Tomography. New York, NY: Springer, 2000.
20. Kelly, T.F. and M.K. Miller. "Atom Probe Tomography." *Review of Scientific Instruments* 78 (2007)
21. FIM and Atom Probe Group, University of Oxford. "Oxford Materials Techniques." *CMS Made Simple*. 1.9.3 <<http://www-fim.materials.ox.ac.uk/techniques.html>>.
22. Schmitz, G., "Atomprobe Analysis of Thin Film Specimens." Institut fur Materialphysik, 2003.
23. Deconihout, B. A. Vella, F. Vurpillot, G. Da Costa, A. Bostel. "3D Atom Probe Assisted by Femtosecond Laser Pulses." *Applied Physics A: Materials Science and Processing* 93 (2008) 995-1003.
24. Miller, M.K. "The Effects of Local Magnification and Trajectory Aberrations on Atom Probe Analysis." *Journal de Physique* (1987) 565-570.
25. Hellman, O.C. and D.N. Seidman. "Measurement of the Gibbsian Interfacial Excess of Solute at an Interface of Arbitrary Geometry Using Three-Dimensional Atom Probe Microscopy." *Materials Science and Engineering*. A327. (2002) 24-28.
26. Brandon, D. and W.D. Kaplan. Microstructural Characterization of Materials. Chichester, England: John Wiley, 2008. Print.

27. Cowley, J.M. "Scanning Transmission Electron Microscopy of Thin Specimens." *Ultramicroscopy*. 2 (1976): 3-16.
28. D.B. Williams, C.B. Carter. Transmission Electron Microscopy. New York. Springer Science Media, Inc, 1996.
29. Kaihola, E.L., J.C. Malaurent, H. Duval and P. Dhez, "The Determination of the Period of Magnetic Multilayers by the X-Ray-Energy Dispersive Diffraction Method." *The Journal of Magnetic Materials*. 93 (1991): 164–168.
30. Karimov, P., S. Harada, H. Takenaka, J. Kawai. "Multilayer Characterization by Energy Dispersive X-Ray Reflectivity Technique." *Spectrochimica Acta Part B: Atomic Spectroscopy*. 62 (2007) 476-480.
31. Arizona State University. "In-Situ Real-Time Atomic Scale Nanostructural Synthesis, Characterization and Modeling." <<http://www.asu.edu/clas/csss/NUE/FIB-Intro.html>>.
32. Giannuzzi, L.A. and F.A. Stevie. "Introduction to Focused Ion Beams." New York. Springer, 2005.
33. Thompson, G.B., Miller, M.K. and Fraser, H.L. "Some Aspects on Atom Probe Tomography." *Ultramicroscopy*. 107.2-3 (2007): 131-139.
34. Miller, M. Atom Probe Tomography: Analysis at the Atomic Level. New York: Kluwer Academic/Plenum Publishers, 2000.
35. Seidman, D. "Three-Dimensional Atom Probe Tomography: Advances and Applications." *Annual Review of Materials Research* 37 (2007): 127-158.
36. Kelly, T.K., Gribb, T.T., Olsen, J.D., Martens, R.L., Shepard, J.D., Wiener, S.A., et al. "First Data from a Commercial Local Electrode Atom Probe (LEAP)." *Microscopy and Microanalysis* 10.3 (2004): 373-383.
37. Thompson, K., D. Lawrence, D. Larson, J. Olson, T. Kelly, and B. Gorman. "In Situ Site-specific Specimen Preparation for Atom Probe Tomography." *Ultramicroscopy* 107.2-3 (2007): 131-39. *Science Direct*. Web.
38. Geiser, B.P., D.J. Larson, S. Gerstl, D. Reinhard, T.F. Kelly, T.J. Prosa, D. Olson. "TipSim." *Microscopy and Microanalysis*. 15 (2009): 302-303.
39. Vurpillot, F. A. Bostel, and D. Blavette. "Trajectory Overlaps and Local Magnification in Three-Dimensional Atom Probe." *Applied Physics Letters* 76 (2000): 3127.
40. Bas, P., A. Bostel, B. Deconihout, D. Blavette. "A General Protocol for the Reconstruction of 3D Atom Probe Data." *Applied Surface Science*." 87 (1995): 298-304.

41. Ziegler, J.F. "The Stopping and Range of Ions in Matter." Pergamon Press. 2-6 (1977-1985)
42. "Periodic Table." *Ask the Editors*. Infoplease. © 2000-2007 Pearson Education, publishing as Infoplease. 11 February 2011 <<http://www.infoplease.com/periodictable.php>>.
43. Hellman, O.C., J.A. Vanderbroucke, J. Rusing, D. Isheim, D.N. Seidman. "Analysis of Three-Dimensional Atom-Probe Data by the Proximity Histogram." *Microscopy and Microanalysis*. 6 (2000): 437-444.
44. Thompson, G.B., R. Banerjee, S.A. Dregia, M.K. Miller, H.L. Fraser. "A Comparison of Pseudomorphic BCC Phase Stability in Zr/Nb and Ti/Nb Thin Film Multilayers." *Journal of Materials Research* 19 (2004): 1582-1590.
45. Marquis, E.A., B.P. Geiser, T.J. Prosa, D.J. Larson. "Evolution of Tip Shape During Field Evaporation of Complex Multilayer Structures." *Journal of Microscopy* (2010)